Advances in Observing Various Coronal EUV Waves in the SDO Era and Their Seismological Applications (Invited Review)

Wei Liu[1,2] · **Leon Ofman**[3,4]

Abstract

Global extreme ultraviolet (EUV) waves are spectacular traveling disturbances in the solar corona associated with energetic eruptions such as coronal mass ejections (CMEs) and flares. Over the past 15 years, observations from three generations of space-borne EUV telescopes have shaped our understanding of this phenomenon and at the same time led to controversy about its physical nature. Since its launch in 2010, the *Atmospheric Imaging Assembly* (AIA) onboard the *Solar Dynamics Observatory* (SDO) has observed more than 210 global EUV waves in exquisite detail, thanks to its high spatio–temporal resolution and full-disk, wide-temperature coverage. A combination of statistical analysis of this large sample, more than 30 detailed case studies, and data-driven MHD modeling, has been leading their physical interpretations to a convergence, favoring a bimodal composition of an outer, fast-mode magnetosonic wave component and an inner, non-wave CME component. Adding to this multifaceted picture, AIA has also discovered new EUV wave and wave-like phenomena associated with various eruptions, including quasi-periodic fast propagating (QFP) wave trains, magnetic Kelvin–Helmholtz instabilities (KHI) in the corona and associated nonlinear waves, and a variety of mini-EUV waves. Seismological applications using such waves are now being actively pursued, especially for the global corona. We review such advances in EUV wave research focusing on recent SDO/AIA observations, their seismological applications, related data-analysis techniques, and numerical and analytical models.

[1] W.W. Hansen Experimental Physics Laboratory, Stanford University, Stanford, CA 94305, USA
[2] Lockheed Martin Solar and Astrophysics Laboratory, Bldg. 252, 3251 Hanover Street, Palo Alto, CA 94304, USA
email: weiliu@lmsal.com
[3] Catholic University of America and NASA Goddard Space Flight Center, Code 671, Greenbelt, MD 20771, USA
[4] Visiting Associate Professor, Department of Geophysics and Planetary Sciences, Tel Aviv University, Tel Aviv 69978, Israel
email: Leon.Ofman@nasa.gov

1. Introduction

The dynamic, magnetized solar corona hosts a variety of waves and wave-like phenomena that are believed to play important roles in many fundamental, yet enigmatic processes, such as corona heating (*e.g.* Ionson, 1978, Heyvaerts and Priest, 1983) and solar-wind acceleration (see reviews by Ofman, 2010 and Cranmer, 2012). Such waves also carry critical information that can be used to decipher otherwise elusive physical parameters of the corona, such as the magnetic-field strength, via a technique called *coronal seismology* (Uchida, 1970; Roberts, Edwin, and Benz, 1984; Nakariakov *et al.*, 1999; Nakariakov and Ofman, 2001; Nakariakov and Verwichte, 2005).

Space-borne extreme ultraviolet (EUV) imagers have been the prime instruments observing traveling coronal disturbances for decades, thanks to a wide range of EUV emission produced by ions at various coronal temperatures. The most spectacular examples are EUV disturbances expanding across a fraction of the solar disk, often in annular shapes and commonly associated with coronal mass ejections (CMEs) and flares. They were discovered by the *Extreme-ultraviolet Imaging Telescope* (EIT: Delaboudinière *et al.*, 1995) onboard the *Solar and Heliospheric Observatory* (SOHO) and rekindled broad interest in large-scale coronal (shock) waves (Moses *et al.*, 1997; Dere *et al.*, 1997; Thompson *et al.*, 1998). They are thus often called "EIT waves", as well as "(global) EUV waves" (Patsourakos and Vourlidas, 2012), "coronal bright fronts" (Gallagher and Long, 2011), or "large-scale coronal propagating fronts" (Nitta *et al.*, 2013). Here we adopt the most commonly used term "EIT waves", while we reserve "EUV waves" for propagating EUV disturbances in general – the subject of the present review.

Over the past decade and a half, three generations of EUV telescopes, notably SOHO/EIT, the *Extreme UltraViolet Imager* (EUVI: Wuelser *et al.*, 2004) onboard the *Solar TErrestrial RElations Observatory* (STEREO: Kaiser *et al.*, 2008), and the *Atmospheric Imaging Assembly* (AIA: Lemen *et al.*, 2012) onboard the *Solar Dynamics Observatory* (SDO: Pesnell, Thompson, and Chamberlin, 2012), have each contributed to shaping our evolving understanding of EIT waves in specific and EUV waves in general. SDO/AIA in particular, as the most advanced solar EUV imager to date, has led to breakthroughs in coronal-wave research. During its 3.5 years of operation, AIA has not only been bringing the long-standing debate on the nature of EIT waves to a closure by establishing a bimodal composition with both wave and non-wave components (Patsourakos and Vourlidas, 2012), but also discovered new types of EUV waves, especially quasi-periodic fast propagating (QFP) wave trains (Liu *et al.*, 2011) and non-linear waves associated with magnetic Kelvin–Helmholtz instabilities (Ofman and Thompson, 2010, 2011; Foullon *et al.*, 2011), adding to the multitude of aspects of this complex phenomenon. Global coronal seismology utilizing these large-scale EUV waves is becoming a reality.

As an active research subject, observations and models of EUV waves have been reviewed extensively in the past, each with a somewhat different focus. Interested readers are referred to Warmuth (2007) for a review based mainly on SOHO and multiwavelength observations, to Wills-Davey and Attrill (2009), Gallagher and Long (2011), and Zhukov (2011) for updates with early STEREO observations, to Patsourakos and Vourlidas (2012) for a synthesized view from SOHO, STEREO, *Hinode*, and SDO in its first year of operation, and to Vršnak and Cliver (2008) and Chen (2011) for related subjects of coronal shocks and CMEs, respectively.

The aim of this review is to summarize the current knowledge of EUV waves, focusing on the unique and revolutionary contributions made by SDO/AIA to observations of three types of waves generally associated with eruptions, *i.e.* EIT waves, QFP wave trains, and small-scale waves including mini-EUV waves and magnetic Kelvin–Helmholtz instability nonlinear waves. We strive to make our review complementary to the existing literature with different perspectives and minimal overlap yet without sacrificing completeness. We review here mainly published material, together with some new results such as structural oscillations of wide-ranging periods triggered by EIT waves, long periodicities of EIT waves themselves, and new clues to the relationship between quasi-periodic wave trains inside and outside CME bubbles (see Figures 6, 7, and 12).

Other types of waves that can be seen in EUV and are generally associated with traditional local coronal seismology are not covered in this review. This is partly because these waves have been extensively studied in the last decade and a half, especially with SOHO and TRACE, while SDO/AIA has not yet made significant advances in their observations. Such waves include standing (oscillations) or propagating magnetosonic waves of slow modes (Ofman *et al.*, 1997; De Moortel, Ireland, and Walsh, 2000), fast kink modes (Aschwanden *et al.*, 1999; Nakariakov *et al.*, 1999; Nakariakov and Ofman, 2001), and fast sausage modes (Nakariakov, Melnikov, and Reznikova, 2003), as well as Alfvén waves (Tomczyk *et al.*, 2007; Jess *et al.*, 2009). Interested readers are referred to relevant reviews (Aschwanden, 2004; Nakariakov and Verwichte, 2005; Banerjee *et al.*, 2007; Roberts, 2008; Ofman, 2009) and recent AIA observations (*e.g.* Aschwanden and Schrijver, 2011; McIntosh *et al.*, 2011; Wang *et al.*, 2012; Gosain and Foullon, 2012; White and Verwichte, 2012; Srivastava and Goossens, 2013; Threlfall *et al.*, 2013).

We organize this article as follows: After a brief description of relevant EUV telescopes in Section 2, we review in Sections 3–5 observations of the three types of EUV waves mentioned above. We then review their coronal seismological applications in Section 6 and related data-analysis techniques and numerical and analytical models in Section 7, followed by conclusions and future prospects in Section 8.

2. Instruments Observing EUV Waves

The evolution of our understanding of EUV waves in the last 15 years has been primarily driven by technological advances of EUV imagers in three generations.

Here we briefly review their capabilities, summarized in Table 1, as well as their outstanding contributions and limitations. Figure 1 shows an example of an EIT wave observed simultaneously by three representative instruments.

Table 1. Capabilities of the recent three generations of EUV imagers.

Instruments	Operation Period	Caden.[1] [seconds]	Expos.[2] [seconds]	FOV	CCD	Resol.,[3] pixel	EUV Channels [Å]
SOHO/EIT	1995–	600	≥ 1.5	$45'^2$	1024^2	$5.2''$, $2.6''$	171, 195, 284, 304
TRACE	$1998-2010$	$20-30$	≥ 15	$8.5'^2$	1024^2	$1.0''$, $0.5''$	171, 195, 284
STEREO/EUVI	2006–	$75-150$	$4-8$	$54'^2$	2048^2	$3.2''$, $1.6''$	171, 195, 284, 304
PROBA2/SWAP	2010–	$60-120$	10	$54'^2$	1024^2	$6.4''$, $3.2''$	174
SDO/AIA	2010–	12	$2-3$	$41'^2$	4096^2	$1.5''$, $0.6''$	94, 131, 171, 193, 211, 304, 335

[1]The highest typical operational cadence. Even higher cadences are generally available (for example, 66 seconds for EIT, 12 seconds for TRACE, and 10 seconds for AIA), but have rarely been used.
[2]Typical exposure.
[3]Angular resolution, pixel size. All instruments, except AIA, have Nyquist-limited resolution at twice the pixel size.

SOHO/EIT has been the primary first-generation EUV wave imager for over a solar cycle. Unfortunately, its operational $12-18$ minute cadence significantly under-samples the typically hour-long lifetimes of EIT waves and results in large uncertainties in their kinematics measurements. Such observations led to under-constrained models and considerable controversy. TRACE (Handy *et al.*, 1999) had much higher cadences of $20-30$ seconds and the best spatial resolution [$1''$] to date, but its small field of view (FOV) made it incapable of tracking global EUV waves and its long exposures can smear rapidly evolving features. As such, TRACE detected only a handful EIT waves during its 12 year mission (*e.g.* Wills-Davey and Thompson, 1999).

STEREO/EUVI, representing the second-generation EUV wave imagers, has alleviated some of the above limitations. It images the full-Sun corona with the largest FOV to date ($54' \times 54'$, up to $r = 1.7\,R_\odot$) from two vantage points, thus offering crucial clues to the 3D geometry (*e.g.* Temmer *et al.*, 2011), especially the height range, of EIT waves within the limitations of optically thin coronal emission. The coronagraphs within the same *Sun Earth Connection Coronal and Heliospheric Investigation* (SECCHI: Howard *et al.*, 2008) package are critical for establishing the CME–EIT wave relationship (*e.g.* Patsourakos and Vourlidas, 2009). However, its common cadence of 150 seconds (occasionally 75 seconds) is inadequate for capturing high-speed waves like QFPs. The *Sun Watcher using Active Pixel detectors and Image Processing* (SWAP: Seaton *et al.*, 2013) instrument onboard the *PRoject for On-Board Autonomy 2* (PROBA2: Santandrea *et al.*, 2013) mission is a derivative of EIT with an improved cadence and FOV similar to EUVI. Its single 174 Å channel provides limited temperature coverage for EUV waves (*e.g.* Kienreich *et al.*, 2013).

SDO/AIA came with revolutionary improvements over previous generations. Its typical cadence of 12 seconds, one to two orders of magnitude higher than
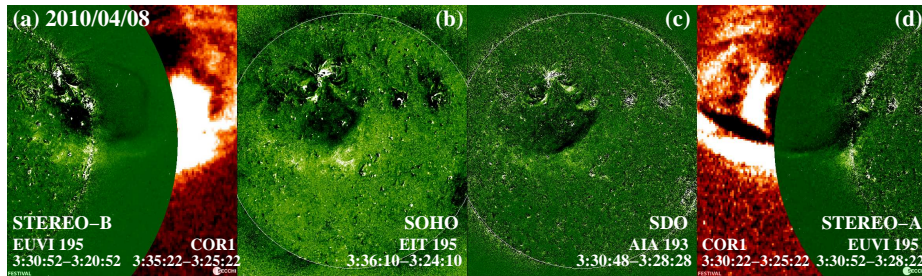
Figure 1. Running-difference images of the 08 April 2010 EIT wave observed by three generations of EUV imagers, SOHO/EIT, STEREO/EUVI (and COR1), and SDO/AIA, at the nearest times from three different viewing angles in near quadrature. STEREO-A and -B were 68° and 71° ahead of and behind the Earth, respectively. The AIA cadence is downgraded to match that of STEREO-A/EUVI. The different image contrasts are mainly due to different cadences of running difference and integration of emission along different lines of sight. Panels c and d are from Liu *et al.* (2010).

those of EIT and EUVI, short exposure of two to three seconds, and high resolution of 1.5″ with 0.6″ pixels are all crucial for detecting fast propagating EUV waves. Its seven EUV channels (including previously underused 94, 131, 211, and 335 Å) cover a wide temperature range, offering unparalleled thermal diagnostic power (O'Dwyer *et al.*, 2010). Its high sensitivity (signal-to-noise ratio) and dynamic range (Boerner *et al.*, 2012) allow for detecting faint waves in the presence of bright emission (*e.g.* flares). In addition, AIA has a high duty cycle of $\geq 95\,\%$ with only interruptions due to eclipses lasting for up to 90 minutes a day for a period of about two weeks once every six months. This enables monitoring the full-Sun corona virtually uninterruptedly and thus significantly increases the detection rate of transients like EUV waves. On the other hand, its $41' \times 41'$ FOV is the smallest among the full-disk EUV imagers in the recent three generations and can miss high-corona features above the limb especially near the Equator. Overall, the combination of unprecedented capabilities makes AIA the best ever instrument for observing EUV waves. By the time of writing, 3.5 years in operation, AIA has detected more than 210 EIT waves (see the list compiled by N. Nitta at http://www.lmsal.com/nitta/movies/AIA_Waves), over 15 QFP wave trains, and various small-scale EUV waves, represented in more than 40 publications.

Other than imagers, EUV spectrometers can provide valuable plasma diagnostics for EUV waves such as the density, temperature, and Doppler and nonthermal broadening velocities (for a review, see Section 8 of Patsourakos and Vourlidas, 2012). Due to the low chance of capturing a transient EUV wave in a narrow slit, *e.g.* with the SOHO/*Coronal Diagnostic Spectrometer* (CDS: Harrison *et al.*, 1995) and the *Hinode/EUV Imaging Spectrometer* (EIS: Culhane *et al.*, 2007), such studies have been performed for only a few events (Harra and Sterling, 2003; Chen and Ding, 2010; West *et al.*, 2011; Harra *et al.*, 2011; Chen *et al.*, 2011a; Veronig *et al.*, 2011; Yang *et al.*, 2013; Long *et al.*, 2013).

3. Global EUV (EIT) Waves

3.1. General Properties from Pre-AIA Observations

Early SOHO/EIT observations indicated that the majority (93 %) of EIT waves are diffuse pulses on the order of 100 Mm wide, while the rest are arc-like, sharp fronts called "S-waves" that eventually become diffuse (Biesecker *et al.*, 2002). EIT waves have a broad speed distribution within $50 - 700 \, \mathrm{km \, s^{-1}}$ (Thompson and Myers, 2009). Their height range was determined by STEREO/EUVI to be one to two gravitational scale heights ($\approx$100 Mm) above the solar surface (Patsourakos *et al.*, 2009; Kienreich, Temmer, and Veronig, 2009). Their counterparts in the high corona up to $r = 3 \, \mathrm{R_\odot}$ were recently imaged in white light by STEREO/COR1 (Kwon *et al.*, 2013b).

EIT waves are associated with a variety of solar activity, including CMEs, Type-II radio bursts, EUV dimmings, stationary brightenings, and remote filament oscillations (see the review by Gallagher and Long, 2011 and references therein). They appear to stop at coronal hole boundaries and avoid active regions (*e.g.* Thompson *et al.*, 1999). Some EIT waves, especially S-waves, are associated with *chromospheric* He I 10830 Å waves (Vršnak *et al.*, 2002; Gilbert *et al.*, 2004) and Hα Moreton waves (Moreton and Ramsey, 1960) which are interpreted as "sweeping skirts" of *coronal* fast-mode (shock) waves (Uchida, 1968). Counterparts of EIT waves at other wavelengths have been imaged in soft X-rays (Narukage *et al.*, 2002; Hudson *et al.*, 2003) and microwave and metric radio bands (Warmuth *et al.*, 2004; White and Thompson, 2005; Vršnak *et al.*, 2005).

3.2. EIT Wave Models and New Constraints from AIA Observations

A number of models were proposed for EIT waves, falling into three categories: wave, non-wave, and hybrid models, as described below and summarized in Table 2. Over the last 15 years, there has been an intense debate between wave and non-wave interpretations, each with its own pros and cons underconstrained by early EIT observations. In recent years, STEREO/EUVI and particularly SDO/AIA have provided new constraints leading to a converged view that includes both wave and non-wave components.

Wave models interpret EIT waves as true waves, most likely *fast-mode magnetosonic waves* (Thompson *et al.*, 1999; Wang, 2000; Wu *et al.*, 2001; Warmuth *et al.*, 2001; Ofman and Thompson, 2002). This explains their quasi-circular shapes, because fast modes are the only MHD waves that can propagate perpendicular to magnetic fields with a weak direction dependence in a low-β plasma such as the solar corona. The measured typical EIT wave speeds of $200 - 400 \, \mathrm{km \, s^{-1}}$ (Thompson and Myers, 2009) and especially the $> 600 \, \mathrm{km \, s^{-1}}$ median speed revealed by AIA (Nitta *et al.*, 2013) are within the expected range of coronal fast-magnetosonic speeds [v_f]. Other supporting evidence established or confirmed by AIA includes quasi-periodic wave trains within broad EIT wave pulses and sequential structural oscillations (*e.g.* Liu *et al.*, 2012), reflections, transmissions, and refractions at structural boundaries (*e.g.* Olmedo *et al.*, 2012),

Table 2. Proposed models for EIT waves and their supporting evidence.

Categories	MHD Wave (Shock)	Non-wave	Hybrid/Bimodal
Models	fast mode slow mode (soliton)	field-line stretching current shell reconnection front	wave + non-wave
Evidence	$v_{EIT} \approx v_f$, deceleration reflection, transmission periodicity, compressibility sequential oscillations Moreton, Type II, SEP assoc.	$v_{EIT} < c_s < v_f$, erratic stationary brightenings[1] long-term dimmings lack of such assoc.	CME–wave decoupling multiple components *plus evidence for wave and non-wave models*

[1]Stationary brightenings favor non-wave models, but can also be explained by wave models (see Section 3.6).

compressional heating and cooling cycles (*e.g.* Downs *et al.*, 2012), cospatial Moreton waves (*e.g.* Asai *et al.*, 2012), and deceleration accompanied by pulse broadening and dispersion (*e.g.* Long, DeLuca, and Gallagher, 2011). EIT waves were also interpreted as *slow-mode shocks* and velocity vortices surrounding CMEs (Wang, Shen, and Lin, 2009) or *slow-mode solitons* formed by a balance between dispersive decay and nonlinear steepening (Wills-Davey, DeForest, and Stenflo, 2007).

Non-wave models interpret EIT waves not as true waves but as signatures of CME-caused reconfiguration of the corona, including plasma compression due to successive stretching of magnetic-field lines (Chen *et al.*, 2002; Chen, Fang, and Shibata, 2005), Joule heating in current shells surrounding CMEs (Delannée, 2000; Delannée *et al.*, 2008), sequential magnetic reconnection between CME flanks and the ambient corona with favorably-oriented field lines (Attrill *et al.*, 2007), or simply line-of-sight (LOS) projection of CME bubbles themselves (Aschwanden, 2009). These alternative models were proposed to resolve difficulties facing the fast-mode wave model, such as erratic kinematics, stationary brightenings, long-lasting dimmings, and some EIT waves being slower than expected fast-mode speeds v_f and even sound speeds c_s. Meanwhile, non-wave models have their own difficulties. For example, the inferred magnetic topology of the quiet Sun does not support a coherently propagating reconnection front (Delannée, 2009).

Hybrid models *including both wave and non-wave components* were suggested to reconcile the above controversy (Zhukov and Auchère, 2004). In this *bimodal* picture, a faster, but often weaker, outer component of a fast-mode wave travels ahead of a generally slower, but stronger inner component of CME-caused reconfiguration. This shift of paradigm has been backed up by increasing evidence from numerical simulations (*e.g.* Downs *et al.*, 2012) and observations especially those from AIA (*e.g.* Liu *et al.*, 2012). The hybrid concept has been widely recognized and incorporated in a coherent picture explaining a broad range of observations (Patsourakos and Vourlidas, 2012, see their Section 11). Another similar attempt to resolve the wave *vs.* non-wave controversy was the recent classification of EIT waves (Warmuth and Mann, 2011; see Section 3.4).

Table 3. AIA observed EIT waves and their characteristics.

Flare			Characteristics[1]				Notes/References
Date	Start GOES	Speed[2]	Bimod.	Heat.	Period.	Refl.	
ddmmyy	Time Class	[km s^{-1}]		Comp.	Oscil.	Tran.	
08Apr10	02:30 B3.7	240	B	H			QFPs (Liu *et al.*, 2010)
12Jun10	00:53 M2.0	360	N				reduced blueshifts (Chen *et al.*, 2011a)
		1280					dome, SEPs (Kozarev *et al.*, 2011)
13Jun10	05:30 M1.0	730		C			dome, SEPs (Kozarev *et al.*, 2011)
		600	W	HC			shock, M_A=1.35 (Ma *et al.*, 2011)
		640		C			$B{\approx}1.4$ G (Gopalswamy *et al.*, 2012)
		600	B	HC			(Downs *et al.*, 2012)
				C			Type II (Kouloumvakos *et al.*, 2014)
27Jul10	08:46 A6.0	560	B				(Chen and Wu, 2011)
14Aug10	09:38 C4.4	420	W				dispersion (Long et al. 2011)
08Sep10	23:05 C3.3	830	B	HC	PO	T	QFPs (Liu *et al.*, 2012)
			B		O		(Gosain and Foullon, 2012)
16Oct10	19:07 M2.9	1390	B		O		(Kumar *et al.*, 2013)
					O		(Aschwanden and Schrijver, 2011)
13Nov10	17:04 B5.7	350	W				surge (Zheng *et al.*, 2013b)
27Jan11	11:53 C1.2	550	B	H	O		(Dai *et al.*, 2012)
14Feb11	17:20 M2.2						Moreton wave (White et al.2011)
15Feb11	01:44 X2.2	730	N	HC	O		curr. shell (Schrijver *et al.*, 2011)
		780	B			RT	(Olmedo *et al.*, 2012)
16Feb11	14:19 M1.6	500	B	C			red/blueshifts (Harra *et al.*, 2011)
		590	W	C			(Veronig *et al.*, 2011)
24Mar11	12:01 M1.0	950	B			T	(Xue *et al.*, 2013)
25Mar11	23:08 M1.0	1020	B		O	RT	(Kumar and Manoharan, 2013)
07Jun11	06:16 M2.5	960	B				(Cheng *et al.*, 2012)
		780	B	H		RT	dome (Li *et al.*, 2012b)
04Aug11	03:41 M9.3	910	W	H	PO	RT	redshifts (Yang *et al.*, 2013)
09Aug11	07:48 X6.9	760	B		O		Moreton wave (Asai *et al.*, 2012)
		1000	B				photosph. (Shen and Liu, 2012c)
					O		(Srivastava and Goossens, 2013)
22Sep11	10:29 X1.4	480		H			M_A=2.4, SEPs (Carley *et al.*, 2013)
24Sep11	09:32 X1.9	690	W		O	R	M_f=1.4 (Shen and Liu, 2012a)
30Sep11	02:46 C1.0	1100	W				jet driven (Zheng *et al.*, 2012a)
23Apr12	17:38 C2.0	960	B			RT	(Shen *et al.*, 2013b)
Range	A$-$X	240$-$1390; speed mean: 740, median: 730, stand. dev: 280 km s^{-1}					
Occurrences[3]			13B	8H	2P	6R	2 Moreton waves
(Total: 21 events, 33 articles)			7W/2N	4C	8O	7T	

Not included: (1) The rest of the 171 AIA events in Nitta *et al.* (2013)

              (2) The six Type-II associated events in Gopalswamy *et al.* (2013)

              (3) The 12 SEP associated events in Park *et al.* (2013)

[1] Abbreviations: B: Bimodal, W: Wave, N: Non-wave; H: Heating, C: Compression; P: Periodicity (of EIT waves), O: Oscillations (triggered by EIT waves); R: Reflection, T: Transmission (or Refraction); according to the original interpretation in the reference.
[2] Maximum speed measured at 193 or 211 Å.
[3] Each event is counted only once in each category.

In the following subsections, we elaborate on the above aspects to which AIA has made key contributions and that are categorized in Table 3 for an exhaustive list of AIA detected EIT waves. Table 4 summarizes AIA updates of EIT-wave properties.

Table 4. EIT-wave properties updated with AIA observations. See Gallagher and Long (2011) and Patsourakos and Vourlidas (2012) for early values and more complete lists.

Properties	Initial Speed	Acceleration	Period	Energy Content
Typical Values	$600 - 700 \, \mathrm{km \, s^{-1}}$	$(-400) - (+300) \, \mathrm{m \, s^{-2}}$	$2 - 70$ minutes	$10^{28} - 10^{29} \, \mathrm{erg}$

3.3. Wave/Non-wave Bimodality and Multiple Fronts
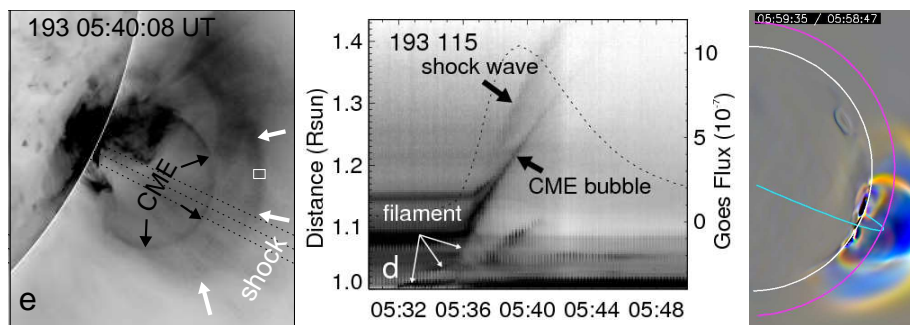
Figure 2. Wave/non-wave bimodality evidenced in a shock running ahead of its CME driver on 13 June 2010 in an AIA 193 Å image (left) and space–time plot from a nearly vertical cut (middle) (from Ma *et al.*, 2011). Right: Simulated composite image (red: 211 Å, green: 193 Å, and blue: 171 Å) for the same event showing a heated outer wave front in yellow followed by a cooling region in blue immediately ahead of an inner CME front (from Downs *et al.*, 2012).

Although multiple fronts are not uncommon in Moreton waves (*e.g.* Narukage *et al.*, 2008) and He I 10830 Å waves (*e.g.* Gilbert and Holzer, 2004), EIT waves were originally considered as a single-pulse phenomenon (Wills-Davey, DeForest, and Stenflo, 2007), This view has recently changed. The first indication of a *bimodal composition* was found in a 2D MHD model (Chen *et al.*, 2002), in which a series of fast-mode waves travel ahead of a CME-driven compression. Chen *et al.* called the former "coronal Moreton waves", ascribing their non-detection to EIT's low cadence, and instead interpreted the latter as an EIT wave. Recent 3D global MHD simulations (Cohen *et al.*, 2009; Downs *et al.*, 2011, 2012) confirmed the composition of an outer fast-mode front and an inner CME compression front. Additional, but non-critical contributions to the inner EUV emission may come from a current shell or magnetic reconnection.

Arguably the first observational evidence of the wave/non-wave bimodality was provided by TRACE and SOHO/CDS (Harra and Sterling, 2003), while other analyses of the same event reached an opposite conclusion favoring a

single pulse (Wills-Davey and Thompson, 1999; Delannée, 2000). More convincing evidence came from quadrature STEREO observations of an EIT wave front decoupling from a CME flank as the latter slows down (Patsourakos and Vourlidas, 2009). Recent AIA observations have established the bimodality as a general trend, as seen in 13 out of 21 EIT waves (see Table 3). One clear example, as shown in Figure 2, is a coronal shock propagating at $600 \, \mathrm{km \, s^{-1}}$ ahead of a slower CME front at $410 \, \mathrm{km \, s^{-1}}$ (Ma *et al.*, 2011). In another example (Chen and Wu, 2011), the slower front decelerates and stops at a separatrix surface, as predicted for field-line stretching (Chen, Fang, and Shibata, 2005). In addition to kinematic differences, the two components can exhibit distinct thermal properties, as discussed in Section 3.8.
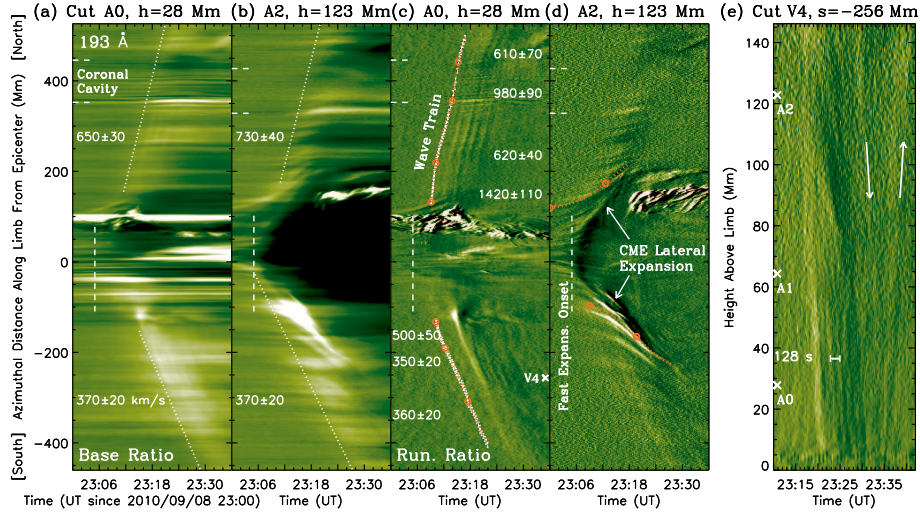

Figure 3. Wave/non-wave bimodality exemplified in a low-corona ($h \lesssim 100 \, \mathrm{Mm}$) quasi-periodic wave train within a broad EIT wave pulse that decouples from the high-corona CME lateral expansion on 08 September 2010 (from Liu *et al.*, 2012). This is evident in AIA 193 Å base-ratio ((a) and (b)) and running-ratio ((c) and (d)) space–time plots from off-limb cuts at two constant heights, and a running-ratio plot (e) from a vertical cut at 256 Mm South of the epicenter. The slanted stripes in (e) indicate delayed arrivals of the wave train at lower heights and thus wave fronts forwardly inclined toward the solar surface. The change of slope near 23:35 from negative to positive is suggestive of an echo or reflection from the underlying chromosphere, as revealed in an MHD simulation (Wang, Shen, and Lin, 2009).

A critical addition by AIA to this bimodal picture is not only one, but *multiple, quasi-periodic fronts* within the outer wave component itself *ahead* of a CME flank, manifesting its true wave nature (Liu *et al.*, 2012). As schematically shown in Figure 12a, such a quasi-periodic wave train comprises low-corona wave fronts forwardly inclined toward the solar surface and travels along it to distances $\gtrsim \mathrm{R_\odot}/2$. In the example shown in Figure 3, there is a dominant two minute period and high initial speeds up to $1400 \, \mathrm{km \, s^{-1}}$. Such wave trains were potentially detected by EUVI at a lower 75-second cadence (Patsourakos, Vourlidas, and Kliem, 2010, see their Figure 11) and resemble simulated coronal

Moreton waves (Chen *et al.*, 2002). Their relationship with QFP wave trains in coronal funnels *behind* CME fronts will be discussed in Section 4.3.

Likewise, the inner non-wave component can contain multiple fronts as well. In the first EIT wave detected by AIA on 08 April 2010 (Liu *et al.*, 2010), *multiple, ripple-like sharp fronts* travel in a wide speed range of $40-240 \, \mathrm{km \, s^{-1}}$ behind a diffuse front at uniform speeds of $200-240 \, \mathrm{km \, s^{-1}}$. Some sharp fronts undergo acceleration, suggestive of being driven by lateral CME expansion. Some faster sharp fronts even overtake slower ones, which, with a hindsight, is possibly due to LOS projection of loops expanding at different heights.

3.4. Kinematics

Kinematics of EIT waves, usually measured at their leading fronts, has a strong bearing on their physical nature. According to a catalog of 176 EIT waves from January 1997 to June 1998 on the early rising phase of solar cycle 23 (Thompson and Myers, 2009), their average speeds are distributed in a wide range of $50-700 \, \mathrm{km \, s^{-1}}$ with typical values of $200-400 \, \mathrm{km \, s^{-1}}$. One cycle later, a new catalog of 171 events detected by SDO/AIA from April 2010 to January 2013 was compiled (Nitta *et al.*, 2013). As shown in Figure 9, a subset of 138 on-disk events has an even broader speed distribution of $200-1500 \, \mathrm{km \, s^{-1}}$ with a *much higher mean* of $644 \, \mathrm{km \, s^{-1}}$, a median of $607 \, \mathrm{km \, s^{-1}}$, and a standard deviation of $244 \, \mathrm{km \, s^{-1}}$. The large lower bound of $200 \, \mathrm{km \, s^{-1}}$ is partly due to the sample selection threshold (angular width $\geq 45°$, travel distance ≥ 200 Mm from the epicenter).

Observational case studies with three generations of EUV imagers have found many EIT waves of nearly *constant speeds* (*e.g.* Ma *et al.*, 2009; Liu *et al.*, 2010) and many others with *decelerations* (*e.g.* Warmuth *et al.*, 2004; Long *et al.*, 2008; Zhao *et al.*, 2011; Xue *et al.*, 2013). A smaller number of events exhibit acceleration and even erratic acceleration and deceleration episodes (*e.g.* Zhukov, Rodriguez, and de Patoul, 2009). Such accelerations often occur at low speeds $\lesssim 200 \, \mathrm{km \, s^{-1}}$, suggestive of a physical connection with CME expansion or filament eruptions. This general trend was confirmed by the new AIA catalog (Nitta *et al.*, 2013) in which more events (57 % *vs.* 43 %) experience deceleration than acceleration. The accelerations, as shown in Figure 4 (right), are compactly distributed around and concentrated below zero, with a mean of $-37 \, \mathrm{m \, s^{-2}}$, a median of $-12 \, \mathrm{m \, s^{-2}}$, and a standard deviation of $162 \, \mathrm{m \, s^{-2}}$, indicating nearly uniform speeds for a large fraction of the events.

A statistical study including 61 events observed by EIT and 17 by EUVI revealed distinct types of EIT waves of possibly different physical origins (Warmuth and Mann, 2011). As shown in Figure 4 (left), the distribution of the initial speed $[v_1]$ *vs.* the average acceleration $[\bar{a}]$ appears to cluster in *three classes*. Class 1 includes fast waves of $\geq 320 \, \mathrm{km \, s^{-1}}$ with stronger decelerations at higher speeds, interpreted as *nonlinear fast-mode* waves or shocks decelerating due to amplitude decay resulting from dissipation and geometric expansion. Class 2 corresponds to waves of moderate and nearly uniform speeds of $170-320 \, \mathrm{km \, s^{-1}}$ with or without slight decelerations or accelerations, interpreted as *linear fast-mode* waves. The final speeds of these two classes fall in a compact range of
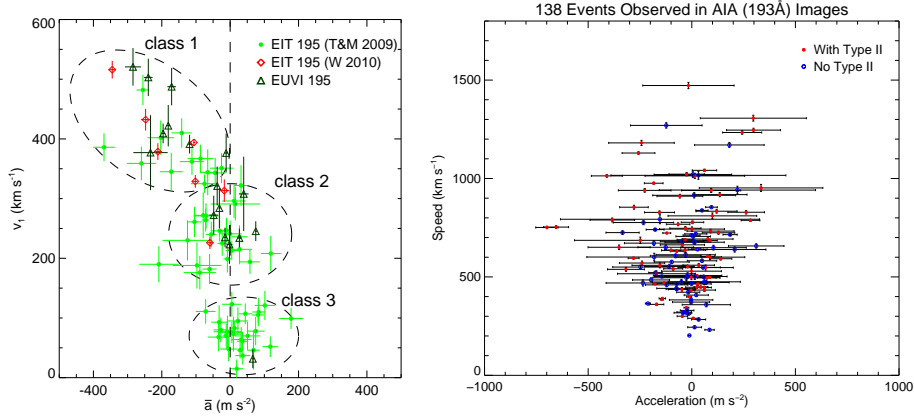
Figure 4. Distributions of EIT wave speeds *vs.* accelerations obtained from EIT and EUVI showing three distinct classes (left; from Warmuth and Mann, 2011) and from AIA appearing more continuously but with some similar trends (right; from Nitta *et al.*, 2013).

$200-300\,\mathrm{km\,s^{-1}}$, similar to the $180-380\,\mathrm{km\,s^{-1}}$ range found by Patsourakos and Vourlidas (2012) from published EUVI and AIA observations. Such final speeds are comparable to the quiet-Sun fast-magnetosonic speeds, further suggesting closely related origins. Class 3 includes very slow waves $\leq 130\,\mathrm{km\,s^{-1}}$ showing constant speeds or slight accelerations, which were interpreted as non-wave, CME-related *coronal reconfiguration*, although slow-mode waves were also suggested (*e.g.* Podladchikova *et al.*, 2010).

These distinct classes cannot be readily identified in the recent AIA ensemble (Nitta *et al.*, 2013; see Figure 4, right), which appears in a more continuous distribution. However, within $450-800\,\mathrm{km\,s^{-1}}$, there is a similar, but weak positive correlation between decelerations and speeds, corresponding to the above Class 1. Events in the $200-450\,\mathrm{km\,s^{-1}}$ range with small absolute accelerations correspond to Class 2, while slow events of Class 3 are left out, partly because of the sample selection thresholds mentioned earlier. We stress that distinct class boundaries are less important than general trends and may not be well-defined at all because of the diversity in physical conditions among different events.

The above classification is not incompatible with the hybrid models. The general presence of both wave and non-wave components can have different observational manifestations that may fall in one of the three classes, depending on specific circumstances. For example, if the stand-off distance between a fast-mode shock and its driving CME is too small to be resolved by an EUV imager, only one component would be detected and identified as a nonlinear shock (Class 1).

The statistical analysis discussed here has its limitations. Each EIT wave is represented by only two numbers, its speed and acceleration, *e.g.* measured in the direction of the highest speed, while other kinematics determining factors, such as the direction (anisotropy), height (*e.g.* speeds increasing with height; Liu *et al.*, 2012; Kwon *et al.*, 2013b), and observing passband or temperature (Long, DeLuca, and Gallagher, 2011), are ignored and should be included in future studies.

3.5. True Wave Behaviors: Reflections, Transmissions, and Refractions

The propagation of any true wave can be altered by the inhomogeneity of its medium and exhibit such behaviors as reflections, transmissions, and refractions at interfaces with strong gradients of the characteristic wave speed. Active regions and coronal holes are regions of high Alfvén and fast-magnetosonic speeds where anomalies of EIT wave propagation take place, as predicted in numerical models (Wang, 2000; Ofman and Thompson, 2002). Early low-cadence observations indicated that EIT waves avoid such regions (Thompson *et al.*, 1998, 1999). EUVI discovered reflections from a coronal hole (Gopalswamy *et al.*, 2009), while AIA provided more definitive evidence of such behaviors.
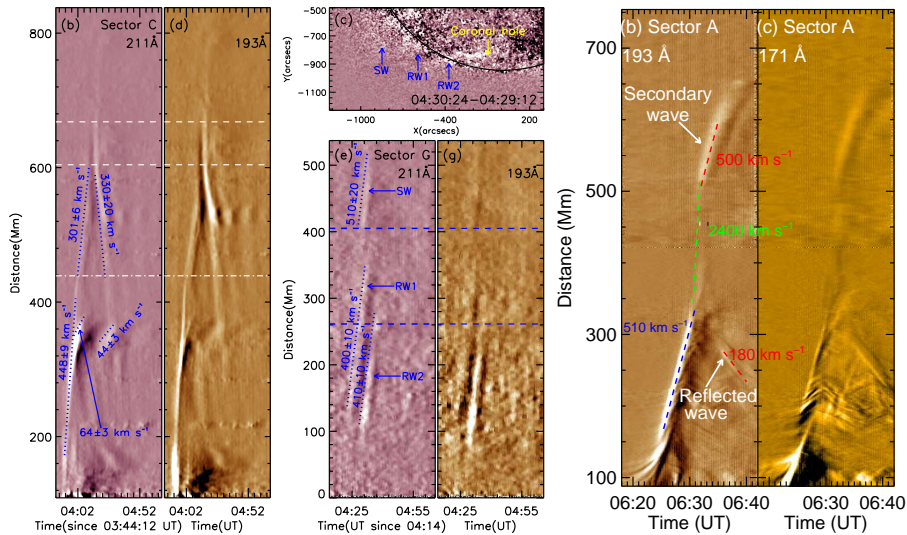
Figure 5. Secondary waves shown in AIA space–time plots on 04 August 2011 (left and middle; from Yang *et al.*, 2013) and 07 June 2011 (right; from Li *et al.*, 2012b). Left: Reflection from a coronal bright point, stationary intensity oscillations (at ≈500 Mm), and loop displacement (at ≈300 Mm). Middle: Double-pulsed reflections (RW1,2) from a polar coronal hole shown in the images on the top and their own secondary wave (SW). Right: Apparent discontinuity or disappearance of a wave inside an active region, implying a high transmission speed of $2400\,\mathrm{km\,s^{-1}}$.

Reflections of EIT waves from various coronal structures, including coronal holes, active regions, and quiet-Sun bright points, have been detected by AIA (Li *et al.*, 2012b; Olmedo *et al.*, 2012; Shen *et al.*, 2013b; Yang *et al.*, 2013). The reported primary waves travel at typically $300-800\,\mathrm{km\,s^{-1}}$ while the reflected waves travel at similar or fractionally lower speeds in the range of $100-500\,\mathrm{km\,s^{-1}}$ (*e.g.* Figure 5, left). Primary and reflected waves share similar thermal properties, such as appearing as brightening at 193 Å but darkening at 171 Å (Li *et al.*, 2012b; Yang *et al.*, 2013), suggestive of a common physical nature. Strong EIT waves can produce cascades of secondary waves by multiple encounters with local structures. For example, the EIT wave associated with the 04 August 2011 M9.3 flare travels more than $1\,\mathrm{R_\odot}$ to reach a polar coronal hole,

where double reflected waves emerge and again produce their own secondary wave when encountering large-scale loops (see Figure 5, middle; Yang *et al.*, 2013). Multiple-pulsed reflections, as modeled numerically (Schmidt and Ofman, 2010), are possible signatures of resonance of the coronal hole in response to the primary wave impact.

A puzzle about reflected EIT waves is that many of them are *fractionally slower* (by up to a factor of four) than the incident waves in the same medium. One possibility is that the incident wave is shocked with a fast-magnetosonic Mach number $M_\mathrm{f} > 1$ while the reflected wave is a linear fast-mode. In addition, the passage of a shock or CME (*e.g.* Gopalswamy *et al.*, 2004) can modify the magnetic and plasma conditions and thus the fast-magnetosonic speed $[v_\mathrm{f}]$ at which a reflected wave will travel. However, for the extreme cases of $1/4$ speed ratio, this would imply a high M_f up to four, indicating a strong shock that would not survive dissipation. We suggest that LOS projection of reflected waves traveling upward at large angles from the solar surface, when viewed from above, could reduce apparent wave speeds and contribute to this discrepancy. Kienreich *et al.* (2013) suggested that in the presence of a bulk plasma flow behind a primary wave traveling in the same direction (*e.g.* the downstream flow of a shock), the reflected wave would propagate through the oppositely directed flow and thus appear at a reduced speed seen in the rest frame.

Transmissions of EIT waves are somewhat more subtle than reflections and have been found in flux-rope coronal cavities (Liu *et al.*, 2012), active regions (Shen *et al.*, 2013b), and corona holes (Olmedo *et al.*, 2012; *cf.* Moreton-wave transmission, Veronig *et al.*, 2006). As expected for higher fast-magnetosonic speeds in these regions, the speeds of the transmitted waves are higher (by $\approx 10 - 60\,\%$) or comparable to those of the incident waves. For example, as shown in Figure 3, the quasi-period wave train has an elevated speed of $\approx 1000\,\mathrm{km\,s^{-1}}$ within the coronal cavity but a lower speed of $\approx 600\,\mathrm{km\,s^{-1}}$ before and after (Liu *et al.*, 2012). Transmissions through topological separatrix surfaces around such structures are strong evidence of a true fast-mode wave component, because a non-wave component related to field line stretching is supposed to stop there (Chen, Fang, and Shibata, 2005).

Another phenomenon that we call "apparent discontinuity" is related to transmission and could be its special case. In the example reported by Li *et al.* (2012b), as shown in Figure 5 (right), when an EIT wave reaches an active region, the primary wave "disappears" or exhibits marginal signals, while a new wave front reemerges from its far side. The authors offered two open interpretations: i) One is a fast-mode wave with a weak signal often below detection transmitting through the active region, as numerically modeled (Ofman and Thompson, 2002), at a high speed up to $2400\,\mathrm{km\,s^{-1}}$, five times the original wave speed. The low signal and high speed are expected due to the strong magnetic field and magnetic pressure/tension of an active region, making it very rigid, which can result in less density or temperature perturbations and thus EUV intensity variations. This can also be explained by *conservation of wave-energy flux*, a product of energy density and group velocity. In general, the relative amplitudes and energy densities of the incident, reflected, and transmitted waves depend on their speeds in the respective media and the incident angle among other

quantities. In addition to energy loss due to reflection and damping, a higher transmission wave speed can lead to an even lower transmission energy density and thus amplitude than those of the incident wave, as manifested in Figure 3c for a flux-rope coronal cavity. ii) Another possibility for "apparent discontinuity" is sequential stretching of neighboring high-altitude magnetic-field lines whose footpoints straddle the active region, causing a jump of a non-wave signal from one side of it to the other (Chen, Fang, and Shibata, 2005). iii) Shen *et al.* (2013b) proposed a third interpretation as wave diffraction around the active region, which, in our view, cannot explain the unusually high speed of "transmission", because it would take a much longer time if the wave were to travel around the active region at the original wave speed on the quiet Sun.

One of the reasons leading to these open possibilities is the ambiguity due to LOS projection onto the solar disk where the height-dependent information is lost and where most of the reported secondary waves were detected. An alternative limb view is needed to recover *height-dependent propagation*, as reported by Liu *et al.* (2014c). They found within an active region a continuous change of the wave-front orientation from forward to backward inclination toward the solar surface, meaning larger wave speeds at lower heights. This is consistent with the expected fall-off of Alfvén and fast-magnetosonic speeds with height in an active region and indicates that the EIT wave indeed transmits through it.

Refraction of EIT waves can be referred to as a subset of transmissions that involve gradual deflections of the wave toward regions of progressively lower wave speeds of an inhomogeneous medium. This is predicted for fast-mode waves by geometric acoustics (Uchida, 1968; Afanasyev and Uralov, 2011) and 3D MHD simulations (Ofman and Thompson, 2002). Observational evidence includes anisotropic lateral propagation avoiding active regions or coronal holes (*e.g.* Thompson *et al.*, 2000, their Figure 5), the change in vertical inclination of the wave front during its traverse through an active region noted above (Liu *et al.*, 2014c), and forward inclinations of the low-corona wave fronts toward the solar surface away from the high corona of greater fast-mode speed [v_f] (*e.g.* Liu *et al.*, 2012; Kwon *et al.*, 2013b; especially during the late stage when the effect of the downward compression of the wave driver diminishes, *cf.* Section 3.10). Near a null point where the magnetic field and Alfvén speed [v_A] approach zero and v_f drops to the sound speed [c_s], refraction can cause a fast-mode wave to wrap around and converge toward it (*e.g.* Figure 2 of McLaughlin and Hood, 2004), but such observations of EIT waves have not been reported. At times, refractions and reflections may be observationally indistinguishable. For example, an EIT wave can be refracted at a large-angle away from an active region, depending on the incident angle and the spatial gradient of v_f, and seemingly appear as a reflection.

Similar to the "apparent discontinuity" in *large* active regions discussed above, a secondary wave can appear ahead of a primary EIT wave that encounters *small* coronal bright points or loops. The former can travel faster than the latter and both co-exist for some time, forming a "bifurcation" shape in space–time plots. Examples have been reported by Li *et al.* (2012b, see their Figures 4 and 5), who interpreted this as evidence of LOS projection of multiple components of refraction at different heights. We suggest another possibility that dispersion

due to the increased inhomogeneity of the medium at such locations can lead to multiple fronts of different speeds (Wills-Davey, DeForest, and Stenflo, 2007). Such open interpretations need to be validated, *e.g.* by numerical simulations.

3.6. Perturbations to Local Structures: Sequential Deflections/Oscillations, Stationary Brightenings, and Sympathetic Eruptions
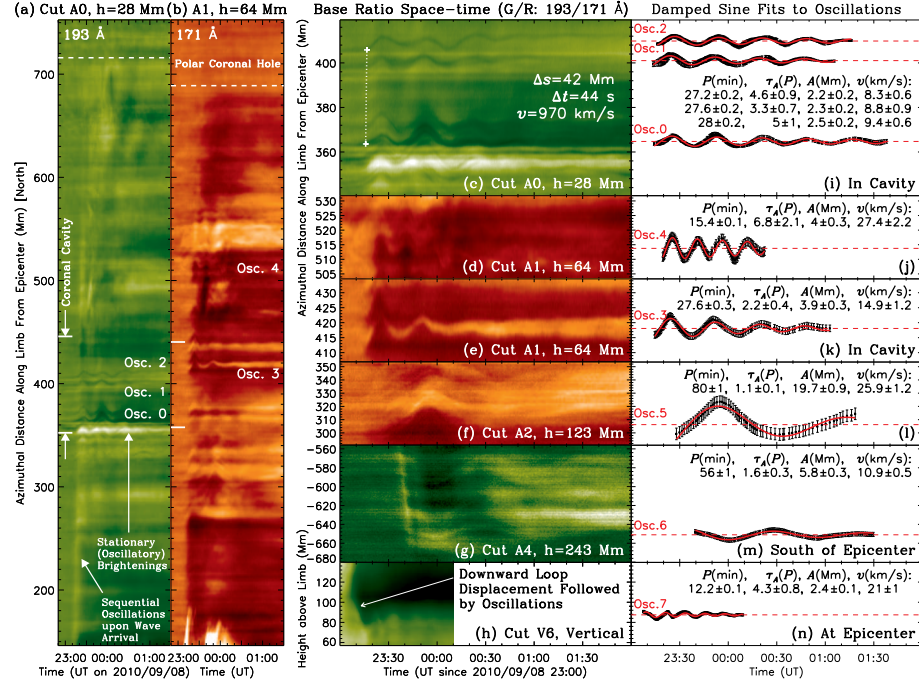

Figure 6. Sequential transverse oscillations set off by the arrivals of an EIT wave at increasing distances on 08 September 2010, shown in base-ratio space–time plots from off-limb cuts at constant heights for 193 Å (a) and 171 Å (b). Note the stationary and oscillatory brightenings at the coronal-cavity boundary. Selected oscillations in enlarged views and their damped sine fits are shown on the right. The fitted period $[P]$, e-folding damping time $[\tau_A]$, and the initial spatial and velocity amplitudes $[A$ and $v]$ are listed. Panels a, c and i are from Liu *et al.* (2012).

AIA's high cadence allows for detection of an unbroken chain sequence of displacements, including **deflections and transverse oscillations**, of local coronal loops set off by an EIT wave (*e.g.* Liu *et al.*, 2012). The delayed onsets of displacements at increasing distances agree with the wave travel times. These displacements, signaling the *first* response to the arrival of a traveling disturbance, are suggestive of its fast-mode wave nature, *i.e.* propagation at the *highest* speed (in the linear regime) supported by the medium. The subsequent oscillations are sustained by a restoring force (dominated by the Lorentz force in a low-β plasma) after the passage of a *transient* perturbation, most like a true wave, rather than a CME expansion or reconnection front that would otherwise cause *permanent* deflections (see Figure 8 of Patsourakos and Vourlidas, 2012).

The example in Figure 6 evidently shows concurrent arrivals of an EIT wave and onsets of oscillations of various local structures. These oscillations occur in a *broad range of periods* – $12-15$ minutes in low-altitude (short) loops, 28 minutes in a filament-hosting coronal cavity, and $56-80$ minutes in high-altitude (long) loops – which are positively correlated with loop lengths and thus suggestive of fast kink modes. They have initial amplitudes of $2-20$ Mm, velocity amplitudes of $8-27\,\mathrm{km\,s^{-1}}$, and e-folding damping times of $1-7$ periods. In another example shown in Figure 5 (left, near $300\,\mathrm{Mm}$), the initial large-amplitude loop displacement appears as a short-lived secondary intensity front that bifurcates from the primary wave and lags *behind* at $\lesssim 1/7$ of its speed. Such fronts differ from the secondary waves at coronal bright points that emerge *ahead* of the primary waves at greater speeds, as mentioned above in Section 3.5.

Oscillations triggered by EIT waves are common in AIA observations, as manifested in 8 out of 21 events listed in Table 3. Other instruments with lower cadences also detected similar but often spatially isolated cases, such as off-limb loop oscillations (*e.g.* Patsourakos and Vourlidas, 2009), filament oscillations (*e.g.* Hershaw *et al.*, 2011; *cf.* those triggered by Moreton waves: Liu *et al.*, 2013), and streamer deflections (*e.g.* Tripathi and Raouafi, 2007; *cf.* those triggered by CMEs: Chen *et al.*, 2010).

Stationary brightenings occur upon arrival or passage of EIT waves at structural boundaries, *e.g.* of active regions, coronal holes, coronal cavities, and quiet-Sun bright points, which can be cospatial with topological separatrices (*e.g.* Delannée and Aulanier, 1999). If no wave signal is detected beyond such a boundary, a stationary brightening or a decelerating secondary front noted above can appear as if an EIT wave came to a stop. This could be the case for low-cadence EIT observations, which may miss (especially faint) reflections or transmissions now clearly seen with AIA. Stationary brightenings can result from persistent heating and/or compression produced by wave or non-wave mechanisms, such as localized energy release triggered by MHD waves (Ofman and Thompson, 2002; Terradas and Ofman, 2004), opening of magnetic-field lines (Delannée, 2000; Chen, Fang, and Shibata, 2005), Joule heating in current sheets (Delannée, Hochedez, and Aulanier, 2007), and continual magnetic reconnection (Attrill *et al.*, 2007). In addition, high-cadence AIA observations revealed *periodic stationary brightenings and darkenings*, indicative of MHD oscillations and waves (*e.g.* Figures 5 and 6, left; Liu *et al.*, 2012, their Figure 9d). In fact, trapped fast-kink modes can be responsible for stationary brightenings at streamer footpoints (Kwon *et al.*, 2013b).

Sympathetic flares and eruptions in general (Becker, 1958; Pearce and Harrison, 1990) have been long thought to be triggered by some waves that carry a disturbance and its energy from one eruption to another. This has been demonstrated in MHD models (*e.g.* Sakai and Washimi, 1982; Ofman and Thompson, 2002). The continuous full-Sun coverage of AIA sparked renewed interest in this topic and revealed profound global connections among large-scale eruptions (Schrijver and Title, 2011; Schrijver *et al.*, 2013). Thus far, very few EIT waves have been identified as triggers of sympathetic eruptions (*e.g.* Khan and Hudson, 2000). Among recent examples observed by AIA are a minor flare induced by an M2 flare across the Equator (Liu *et al.*, 2014a) and high-speed

$(200-400 \, \mathrm{km\, s^{-1}})$, low-corona mass ejecta in a wide angular range (Liu *et al.*, 2014c). A statistical survey is yet to be carried out to determine how common such sympathy is and what role EIT waves play.

3.7. EIT Wave Periodicity

As EIT waves were largely considered as a single-pulse phenomenon in the past (Wills-Davey, DeForest, and Stenflo, 2007), very little attention was paid to their possible periodicities. The only prior detection, to the best of our knowledge, was a traveling 195 Å intensity oscillation with an average period of about seven minutes found by Ballai, Erdélyi, and Pintér (2005) in the extensively studied 1998 June 13 TRACE event (*e.g.* Wills-Davey, 2006). Now, AIA has revealed a variety of periodicities pertinent to the true wave components of EIT waves, reflecting the characteristics of their *drivers* and *media*.
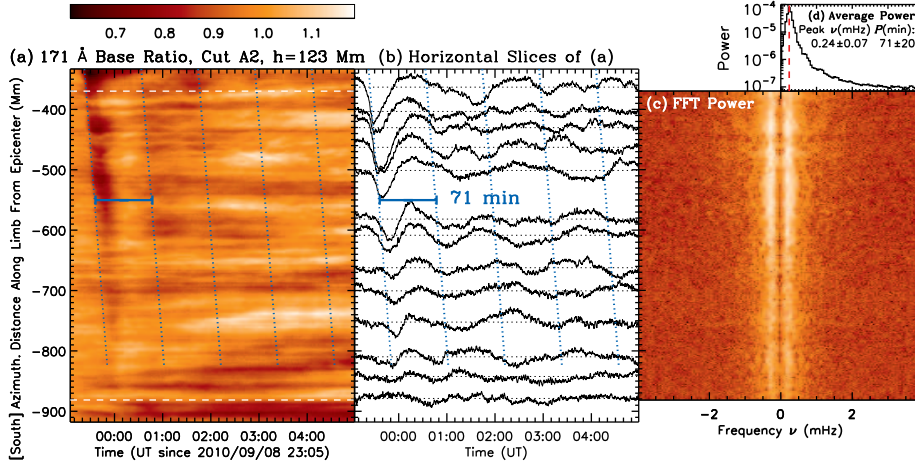

Figure 7. Multiple-pulsed, long-period traveling intensity oscillations of the EIT wave on 08 September 2010 (Liu *et al.*, 2012). (a) Base-ratio space–time plot at 171 Å from azimuthal off-limb cut A2 to the South of the eruption where the quiet Sun is relatively homogeneous. (b) Temporal profiles from horizontal slices of (a) at selected distances marked by the black-dotted line. The slanted lines indicate propagating pulses at a dominant period of 71 ± 20 minutes. (c) Fourier power of the temporal profiles at each distance in (a) within the range marked by the two white dashed lines. (d) Average Fourier power ($\nu \geq 0$ only) by collapsing (c) in distance.

For example, the EIT wave trains shown in Figure 3 have a broad period range of $36-212$ seconds (Liu *et al.*, 2012). The dominant two minute period matches X-ray flare pulsations, but is well below the $12-80$ minute periods of local oscillations on the wave path (see Figure 6). This suggests a *periodic driver* related to flare pulsations that determines the wave periods. This and other potential periodicity contributors, including a dispersive medium, will be discussed in Section 4.2.

The *medium* through which EIT waves propagate, namely the solar corona, can further modify their periods if they represent propagating eigenmode oscillations due to MHD resonances. At first glance, this seems unlikely, because the

corona is inhomogeneous and threaded by magnetic structures of a wide range of characteristic periods, as shown in Figure 6. However, this may happen under favorable conditions.

One example was found from our additional analysis of the event presented in Liu *et al.* (2012). As shown in Figure 7, the passage of the EIT wave produces an initial darkening at 171 Å followed by multiple cycles of intensity oscillations that generally decrease with time and distance in amplitude. The periods are on the order of one to two hours and some oscillations exhibit more than one period, which could result from LOS superpositions of multiple off-limb structures. One can identify a series of coherent wave pulses traveling over 500 Mm with a dominant period of 71 ± 20 minutes that translates into a wavelength of 1400 Mm or $2\,\mathrm{R_\odot}$, considering the measured wave speed of $330\,\mathrm{km\,s^{-1}}$. Such traveling oscillations last for six hours, meaning that the global corona is left undulating for a long time after being swept by the initial wave. This further points to the global nature of EIT waves and solar eruptions (*e.g.* Zhukov and Veselovsky, 2007; Schrijver *et al.*, 2013).

As to the origin of such *coherent long periods*, one possibility is collective kink oscillations of large-scale loops of similar lengths and thus periods, such as vertical kink modes in trans-equatorial loops (Zaqarashvili *et al.*, 2013) and those trapped in streamers (Kwon *et al.*, 2013b). Another, yet less likely, possibility is fast magnetosonic–gravity surface waves (Ballai, Forgács-Dajka, and Douglas, 2011), provided a vertical density jump lies in an everywhere-vertical magnetic field, for which no observational evidence has been found.

3.8. Thermal Properties

Thermal properties of EIT waves are inferred from observations with multiple passbands each covering a specific temperature range of the emitting plasma. The seven EUV channels of AIA have significantly increased the temperature coverage, which now ranges from ≈ 0.08 MK (304 Å) in the transition region to $\gtrsim 10$ MK (131 and 193 Å) in flares (O'Dwyer *et al.*, 2010). In general, EIT waves are best seen as intensity enhancements in the 193 and 211 Å channels that have peak temperature responses at 1.6 and 2.0 MK, respectively, but as intensity reductions in the 171 Å channel that peaks at 0.8 MK. This anti-correlation indicates *plasma heating* taking place between 0.8 and $1.6-2.0$ MK, consistent with similar trends seen by TRACE (Wills-Davey and Thompson, 1999) and EIT (Gopalswamy and Thompson, 2000). In other channels, intensity enhancements become progressively weaker from 335 to 94, 131, and 304 Å.

There are exceptions to this general trend. First, not all EIT waves are 171 Å dark. As shown in Figure 9d, among 138 events observed by AIA, 17 % appear as 171 Å bright, 41 % as dark, and the rest with no clear signal. 171 Å brightening indicates a *low temperature* $[\lesssim 0.8$ MK] of the pre-event plasma or a *strong density enhancement* (*e.g.* at a CME front) dominant over temperature effects. In fact, in the high speed regime $\gtrsim 900\,\mathrm{km\,s^{-1}}$, there are relatively more 171 Å bright waves, which are likely shocks with strong compression. An opposite trend was found in 34 EIT waves observed by EUVI (Nitta *et al.*, 2014b) with 59 % bright and only 18 % dark. One possible explanation is that these EUVI events occurring

during the extended solar minimum could have different environments, *e.g.* lower temperatures or weaker magnetic fields, compared with those AIA events during the rise phase of the present solar cycle.

Another exception is that the 193 Å wave signal is not always bright, although this trend persists in all of the AIA events reported by Nitta *et al.* (2013). For example, two recent homologous EIT waves both appear dark at 171 and 193 Å, but bright at 211 and 335 Å, suggesting a *high initial temperature* in the 1.6 – 2.0 MK range (Liu *et al.*, 2014a). Among other examples are 195 Å-dark wave fronts detected by EIT (Zhukov and Auchère, 2004; their Figure 2) and EUVI (Nitta *et al.*, 2014b; their Table 2).
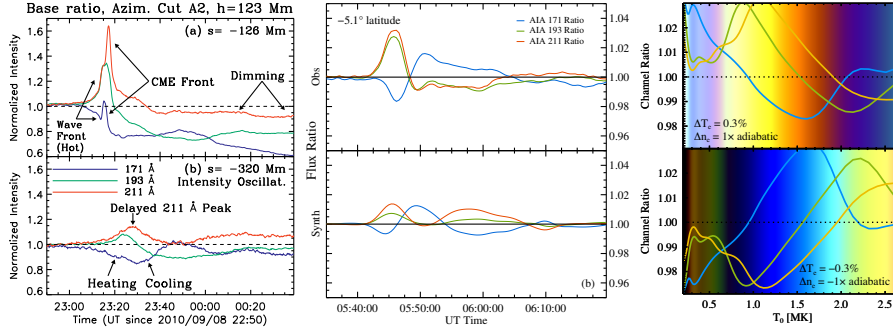

Figure 8. Thermal properties of EIT waves. Left: AIA intensity variations on 08 September 2010 at two locations on the EIT wave path showing distinct thermal characters of the wave and non-wave components (top) and delay across passbands and oscillations (bottom) (from Liu *et al.*, 2012). Middle: Observed (top) and simulated (bottom) AIA intensity variations on 13 June 2010 showing multiple heating and cooling cycles. The left and middle panels share the same color scheme for passbands. Right: Predicted fractional intensity changes of AIA channels (blue: 171 Å, green: 193 Å, orange: 211 Å) for adiabatic heating (top) and cooling (bottom) as a function of the initial temperature [T_0]. The background is the combined tri-color signal at each T_0. The middle and right panels are from Downs *et al.* (2012).

As shown in Figure 8 (middle), after the general initial heating phase with brightening at 193 and 211 Å and darkening at 171 Å, a cooling phase follows with reversed intensity variations. This can be explained by adiabatic heating due to compression followed by cooling with subsequent expansion/rarefaction driven by a restoring pressure gradient force. Mild adiabatic compression was estimated to cause $\approx 10\%$ increases in both density and temperature for the EIT wave associated with the 15 February 2011 X2.2 flare (Schrijver *et al.*, 2011). Such compression-expansion is consistent with the red-blueshift sequence detected by *Hinode*/EIS in coronal lines (Harra *et al.*, 2011; Veronig *et al.*, 2011), similar to the well-known down-up swings in chromospheric Hα Moreton waves. Post-EIT wave cooling can continue even after the perturbed plasma returns to the initial temperature, unexpected for conductive cooling. The observed cooling timescales on the order of ten minutes are significantly shorter than radiative cooling times in the quiet Sun, which are typically orders of hours (*e.g.* Liu, Berger, and Low, 2012). Such behaviors, however, agree with *multiple cycles of adiabatic compression and expansion* of a compressible, fast-magnetosonic wave. Wave dissipation may also contribute to the initial heating.

AIA's rapid cadence allows for tracking detailed temporal evolution of thermal structures. For example, as shown in Figure 8 (upper left), a thin layer with the general anti-correlation between 193/211 Å and 171 Å, indicative of heating, is followed by a sharp brightening and then prolonged dimming in all three channels, indicative of density enhancement and depletion, respectively. This suggests a heated and compressed sheath of a (shocked) wave component preceding a non-wave component of CME expansion, each with *distinct thermal characters*. There is a delay of the maximum intensity variations at 211 and 171 Å from that at 193 Å (Figure 8, lower left), which could be related to passband-dependent wave kinematics (Long, DeLuca, and Gallagher, 2011). In a coronal shock imaged by AIA, Ma *et al.* (2011) found similar *delays indicative of progressive heating* and ionization to higher charge states. They inferred a temperature of 2.8 MK in qualitative agreement with the result from differential-emission-measure analysis of the same event (Kozarev *et al.*, 2011).

3.9. Pulse Evolution: Amplitude and Width

The evolution of the pulse shape, or so-called perturbation profile, can give additional clues to the nature of EIT waves. The pulse shape is usually measured with the EUV intensity profile as a function of distance or time. It often appears as a hump that can be fitted with a Gaussian and characterized with an amplitude [A] and full-width half maximum [FWHM].

Early observations of a few EIT waves by TRACE within its limited FOV suggested a dispersionless behavior, *i.e.* the wave pulse maintains its coherence without increase in FWHM (Wills-Davey, 2003). This was interpreted as evidence of solitons (Wills-Davey, DeForest, and Stenflo, 2007). However, EIT observations indicated a more general trend of *amplitude decay and pulse broadening* often accompanied by wave deceleration, which is consistent with a non-linear fast-magnetosonic wave or shock degenerating into a linear wave due to dispersion, dissipation, and geometric expansion (*e.g.* Warmuth, 2010). EUVI added that the amplitude sometimes grows for a few minutes prior to its decay and the FWHM often increases from $\approx$50 to 200 Mm over the course of the event (Veronig *et al.*, 2010; Muhr *et al.*, 2011; Long *et al.*, 2011; Li *et al.*, 2012a).

AIA brought more details, some unexpected, to this general picture. Liu *et al.* (2010) found in certain directions an increase followed by a decrease in pulse amplitude that is anti-correlated with the FWHM, implying pulse steepening follow by broadening. In other directions, the pulse amplitude decreases linearly with distance r, which is faster than a surface wave ($A \propto r^{-1}$) but slower than a spherical wave ($A \propto r^{-2}$) due to geometric expansion alone. This is compared to earlier dependencies of r^{-1} found by TRACE (Wills-Davey, 2003) and $r^{-2.5\pm0.3}$ by EUVI (Veronig *et al.*, 2010). These results imply *complex interplay between dispersive decay and nonlinear steepening*. Long, DeLuca, and Gallagher (2011) found passband-dependent intensity enhancements (amplitudes) ranging from 10 % at 304 Å to 90 % at 211 Å. By fitting perturbation profiles with sinusoidal waves within a Gaussian envelope, they obtained pulse expansion rates of $\approx$200 km s^{-1} and dispersion rates of $\mathrm{d}^2\omega/\mathrm{d}k^2 \approx 10\,\mathrm{Mm}^2\,\mathrm{s}^{-1}$.

The common practice using *intensity-perturbation profiles* must be applied with care for a number of reasons: Because of the inhomogeneity of the corona

and LOS integration of optically thin EUV emission, each image pixel can contain contributions from unrelated structures, *e.g.* each with its own periodicity (see Section 3.6), which can lead to complex temporal variations. This can be further complicated by multiple (wave and non-wave) components, wave periodicities, and thermal effects (see Sections 3.3, 3.7, and 3.8). Some refinements have been adopted to mitigate such impacts, for example, by excluding the trailing side of a perturbation profile from Gaussian fits to avoid the non-wave contribution such as dimming (Muhr *et al.*, 2011).

3.10. Generation of EIT Waves

It has been established that it is CMEs (large-scale), not flares (localized), that generate EIT waves traveling across the solar disk (*e.g.* see Section 3.11; Warmuth, 2007; Vršnak and Cliver, 2008; Zhukov, 2011). Specifically, the **lateral expansion** of the flank of a CME was recently recognized to play an important role (for a review, see Section 10 of Patsourakos and Vourlidas, 2012). There has been strong supporting evidence from EUVI and AIA observations (*e.g.* Patsourakos, Vourlidas, and Stenborg, 2010; Temmer, Vršnak, and Veronig, 2013) and numerical or analytical models (*e.g.* Pomoell, Vainio, and Kissmann, 2008; Temmer *et al.*, 2009). A lateral inflation or over-expansion is characterized by a faster growth of a CME bubble in the lateral than in the radial direction. The latter is critical to generating an upward propagating (shock) wave in the high corona, but less relevant to an on-disk EIT wave. When a CME expands rapidly enough in all directions, a dome-shaped EIT wave can be detected (*e.g.* Veronig *et al.*, 2010; Li *et al.*, 2012b).

A **downward compression**, in addition to the lateral CME expansion, can also be important. As schematically shown in Figure 12a, Liu *et al.* (2012) found the onset of an EIT wave being associated with the downward expansion of a growing CME bubble originally centered at an elevated height of ≈ 100 Mm. This can happen when a CME self-expands faster than the rise of its center. It pushes the low-corona plasma against the underlying chromosphere, resulting in *enhanced compression efficiency*. A narrow angle formed between the forwardly inclined lower portion of a laterally expanding CME bubble and the chromosphere underneath it has a similar effect. It may contribute to such EIT wave characteristics as i) initial redshifts followed by blueshifts (Veronig *et al.*, 2011), ii) the forward inclination of the early, low-corona wave front toward the solar surface, and iii) the dominance of wave signals at lower heights $\lesssim 100$ Mm over CME expansions (Liu *et al.*, 2012).

The *impulsiveness* of the CME lateral expansion, characterized by its *acceleration*, is key to EIT wave generation (Patsourakos and Vourlidas, 2012). This is backed up on theoretical grounds that pistons with greater and/or more prolonged accelerations tend to produce stronger nonlinear waves or shocks (see Vršnak and Cliver, 2008 for a review). EIT waves often first appear at considerable distances of ≈ 100 Mm from the epicenter, delayed by a few minutes from the initiation of the rapid CME expansion (*e.g.* Liu *et al.*, 2012). Such space–time delays allow the lateral expansion to reach speeds of several hundred $\mathrm{km\,s^{-1}}$ with accelerations up to a few hundred $\mathrm{m\,s^{-2}}$, and thus to build up

sufficient compression to the ambient corona to produce detectable EUV signals, as predicted for shock formation (*e.g.* Žic *et al.*, 2008; see Section 7.2).

There is a noticeable trend that, regardless of the associated CME final speeds or flare sizes, eruptions without appreciable lateral expansion (or with but non-impulsive) tend to produce no or weak on-disk EIT-wave signatures. Examples include quiescent filament eruptions moving mainly radially with gentle acceleration profiles. Future statistical analysis of the quantitative relationship between the CME lateral expansion and EIT-wave formation is required.

3.11. Association With CMEs and Flares

It has been widely recognized that CMEs, especially fast and wide ones, are closely related to EIT waves and serve as a necessary but not sufficient condition (Biesecker *et al.*, 2002). For example, there were five times more front-side CMEs than EIT waves during a 13-month period (Cliver *et al.*, 2005). Recent AIA observations indicated that their association is *not as strong as previously thought* (Nitta *et al.*, 2013). As shown in Figure 9b, although faster EIT waves still tend to be associated with stronger CMEs, more than 1/3 of the 138 waves are associated with weak outflows reaching heliocentric distances $\leq 5\,R_{\odot}$ (labeled CME level 1) that are not typical, large-scale CMEs with three-part structures (Hundhausen *et al.*, 1984; Schwenn, 1996). Meanwhile, the correlation between on-disk EIT wave speeds and radial CME speeds, although positive, is very weak (see Figure 8 of Nitta *et al.*, 2013). These results are not surprising because lateral and radial expansions of CMEs are not necessarily correlated and, as stressed above, it is the early-phase lateral expansion in the low corona (often below the FOVs of CME-detecting coronagraphs) that is more relevant to EIT wave generation.

The association of EIT waves with flares is generally considered weak. For example, no EIT wave was detected in 14 major flares without CMEs (Chen, 2006), and about 50 % of 176 waves were associated with minor flares of B-class or lower (Cliver *et al.*, 2005). At times, flare energy release is too late, too little to account for EIT waves (*e.g.* Veronig, Temmer, and Vršnak, 2008). These results contradict the interpretation of EIT waves as blast waves generated by impulsive flare heating. On the other hand, as shown in Figures 9a and 9b, there are similar "normal" type speed distributions of AIA-detected waves in association with flares and CMEs. That is, the mid-class flares (C and M) and CMEs (levels 2 and 3) correspond to the majority of the EIT waves of intermediate speeds. There is a tendency of association of faster EIT waves with stronger flares and CMEs, which implies an *energetic correlation* between these three phenomena that are integral components of typical solar eruptions.

3.12. Association With Moreton Waves, Type-II Bursts, and SEPs

Chromospheric Hα Moreton waves are strongly associated with a subset of EIT waves, *i.e.* those sharp, well-defined "S-waves" (Wills-Davey and Attrill, 2009 and references therein) and Type-II radio bursts (Vršnak and Cliver, 2008). Their overall degree of correlation with EIT waves, considering both sharp and
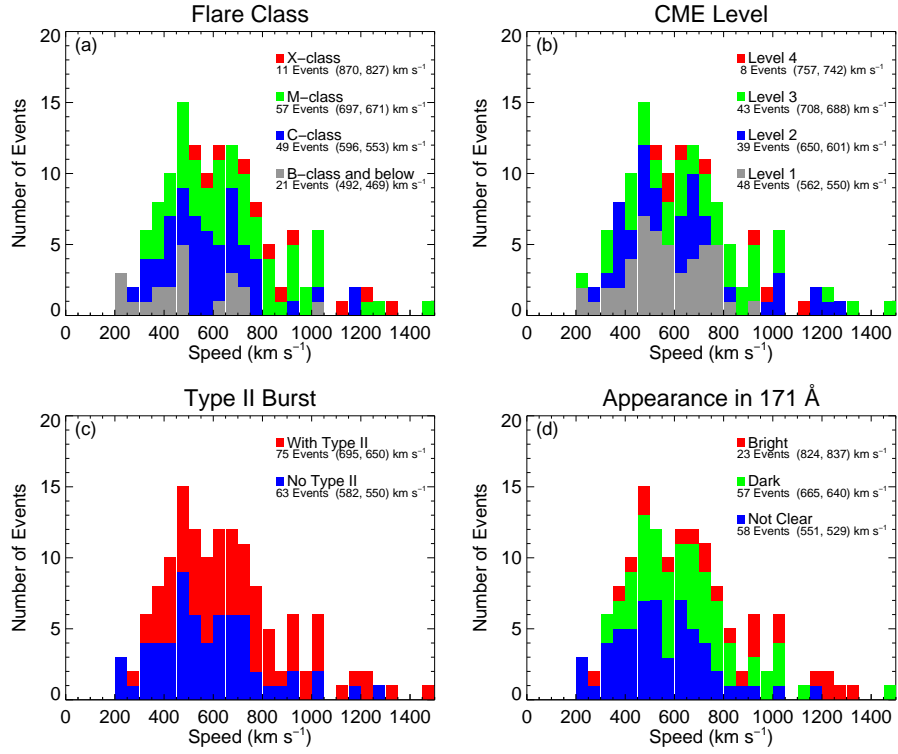
Figure 9. Histograms of speeds of 138 on-disk EIT waves observed by AIA, with breakdowns in flare class, CME level, radio Type-II burst association, and 171 Å wave signal. The mean and median speeds of each category are listed (from Nitta *et al.*, 2013).

diffuse types, is low, with only 1 % in 173 events (Biesecker *et al.*, 2002) and 21 % in 14 events of simultaneous EIT and Hα observations associated with ≥ M-class flares (Okamoto *et al.*, 2004). Moreton waves have much *narrower angular widths* than their EIT-wave counterparts, *e.g.* with a mean of 92° *vs.* 193° in 13 events (Zhang *et al.*, 2011). Early case studies (*e.g.* Warmuth, 2010) indicated that a fast-mode shock undergoing deceleration and decay can produce both a Moreton wave of typically $500-1000 \, \mathrm{km \, s^{-1}}$ and a fractionally slower EIT wave in the late stage. The high median wave speed $> 600 \, \mathrm{km \, s^{-1}}$ revealed by AIA (Nitta *et al.*, 2013) suggests that EIT waves can be detected in early stages as well. During the 9 August 2011 X6.9 flare, cospatial wave fronts at initial speeds of $800-1000 \, \mathrm{km \, s^{-1}}$ were detected from the upper photosphere to the corona in Hα and AIA's UV (1700 and 1600 Å) and EUV channels (Asai *et al.*, 2012; Shen and Liu, 2012c). On the other hand, the forward inclination of an EIT wave front in the low corona implies a *delay* of up to minutes of a Moreton wave from its coronal counterpart (Afanasyev and Uralov, 2011; Liu *et al.*, 2012), consistent with the analysis of the Moreton wave during the 14 February 2011 M2.2 flare (White, Balasubramanian, and Cliver, 2011).

It presents a challenge to draw a general conclusion on the Moreton–EIT wave relation, because Moreton waves have been *rarely observed*, *e.g.* only two reported to date in the SDO era, in contrast to more than 210 EIT waves. Aside from noncontinuous ground-based Hα coverage, this two orders of magnitude difference in detection rate suggests that some *more stringent conditions* are required for Moreton waves than ordinary EIT waves. Such conditions, *e.g.* a strong shock with Mach number > 2 (Balasubramaniam, Pevtsov, and Neidig, 2007), must be able to produce a compression strong enough to penetrate deep down to the chromosphere. It was proposed that He I 10830 Å waves formed in the upper chromosphere could be a link between coronal EIT waves and chromospheric Moreton waves (Vršnak *et al.*, 2002), but the rarity of such observations and the complexity of line formation present another challenge (*e.g.* Gilbert *et al.*, 2004). Moreton waves should not be confused with sequential chromospheric brightenings along narrow channels without a well-defined wave front, ascribed to electron precipitation from high-corona magnetic reconnection (Balasubramaniam *et al.*, 2005).

Metric Type-II radio bursts are signatures of coronal shocks that are more often considered to be driven by CMEs than by flares (Vršnak and Cliver, 2008). A Type-II burst is generally accepted as a sufficient but not necessary condition for an EIT wave. 90 % of the type IIs during 1997 were associated with EIT waves (Klassen *et al.*, 2000), while only 29 % of the 173 EIT waves from 1997-Mar to 1998-Jun were associated with Type IIs, with somewhat higher correlation rates at disk center and the limb than at intermediate longitudes (Biesecker *et al.*, 2002). As shown in Figure 9c, 54 % of the 138 AIA-detected waves (Nitta *et al.*, 2013, 2014a) were accompanied by Type IIs and had a slightly higher median speed (650 *vs.* 550 $\mathrm{km\,s^{-1}}$) than Type-II free waves. Faster EIT waves with speeds $\gtrsim 800\,\mathrm{km\,s^{-1}}$ have stronger associations with Type IIs, implying a common shock origin. Meanwhile, there are Type-II free, but fast EIT waves, which, like radio quiet, but fast and wide CMEs (Gopalswamy *et al.*, 2008), may be due to large fast-mode speeds of the ambient corona, making shock formation difficult, or due to large angles of the wave-driving eruptions from the Sun–observer line. Recently, Kouloumvakos *et al.* (2014) reported a Type-II burst originating from the sheath between a CME bubble and a preceding shock in both radial and lateral directions.

Solar energetic particles (SEPs) are generally considered to be accelerated by CME shocks and/or flares (see Reames, 2013 for a review). In the last two decades, there has been increasing evidence of correlation between SEPs and Moreton and/or EIT waves (*e.g.* Kocharov *et al.*, 1994; Torsti *et al.*, 1999; Krucker *et al.*, 1999), suggesting an association of such waves with shocks. Recent efforts were made to identify a possible spatio–temporal correlation between the releases of SEPs and the arrivals of EIT waves at their source regions connected by open magnetic-field lines to observers at multiple viewpoints (*e.g.* Kozarev *et al.*, 2011; Rouillard *et al.*, 2011, 2012; Nitta, 2012; Park *et al.*, 2013; Miteva *et al.*, 2014). However, their physical relation has yet to be established. Open questions include whether the flank of a CME-driven shock in a quasi-perpendicular orientation, likely manifested as a low-corona EIT wave, or the

high-corona nose of the shock in a quasi-parallel orientation is more important in accelerating and/or transporting SEPs. It was predicted that very fast ($\gtrsim 1000\,\mathrm{km\,s^{-1}}$) shocked EIT waves, missed by previous instruments, can be responsible for rapid onsets of some SEPs including ground level events (Nitta *et al.*, 2012). This can be potentially verified with high-cadence AIA data.
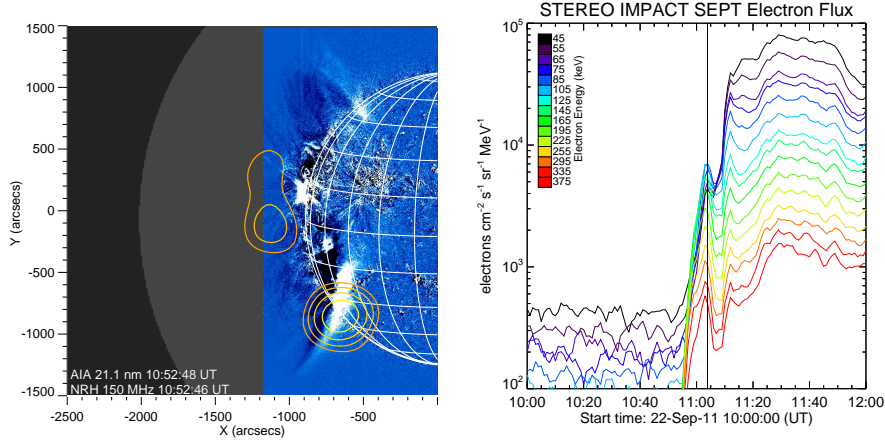

Figure 10. Left: Cospatial EIT wave front in an AIA 211 Å image and 150 MHz contours from the Nançay radioheliograph (NRH) traveling along the solar limb on 22 September 2011. Right: Energetic electron fluxes at $45-375$ keV detected by the *Solar Electron Proton Telescope* on STEREO-B (from Carley *et al.*, 2013; reproduced by permission of the Nature Publishing Group).

Figure 10 shows an example of a joint study of an EIT wave, radio bursts, and SEPs (Carley *et al.*, 2013). In this event, a cospatial EIT wave front and 150 MHz source propagate parallel to the solar surface, interpreted as a CME-flank-driven, quasi-perpendicular shock that efficiently accelerate electrons which produce the observed plasma emission.[1] Energetic electrons producing a Type-III burst are detected *in-situ* at their expected arrival time (marked by the vertical line, right panel). A followup study further indicated that the Type-II-burst associated shock forms at the CME flanks where the inferred Alfvén-speed map shows a local minimum (Zucca *et al.*, 2014).

4. Quasi-periodic Fast Propagating (QFP) Wave Trains

4.1. General Properties: Morphology and Kinematics

Quasi-periodic fast propagating (QFP) wave trains were one of the serendipitous discoveries of SDO/AIA (Liu *et al.*, 2010; Liu *et al.*, 2011) and are strong evidence of quasi-periodic fast-mode magnetosonic waves. As shown in Figure 11 (left),

---

[1] A similar metric radio source associated with a Moreton–EIT wave was reported by Vršnak *et al.* (2005) and alternatively interpreted as optically thin gyrosynchrotron emission.

they usually appear as a series of arc-shaped, $1-5\%$ intensity variations emanating from flare kernels in active regions and traveling upward along *funnel- or conic-shaped paths* within narrow angles (say, $10° - 60°$) often outlined by coronal loops. They propagate at *high speeds* of $500 - 2200\,\mathrm{km\,s^{-1}}$ up to $200 - 400\,\mathrm{Mm}$ from their origins, and can last episodically from about ten minutes to more than one hour with numerous pulses following one another. These characteristics distinguish QFP wave trains from comparably slower EIT waves that propagate in wider angular extents to greater distances across the solar disk or Moreton waves that travel on the chromosphere.
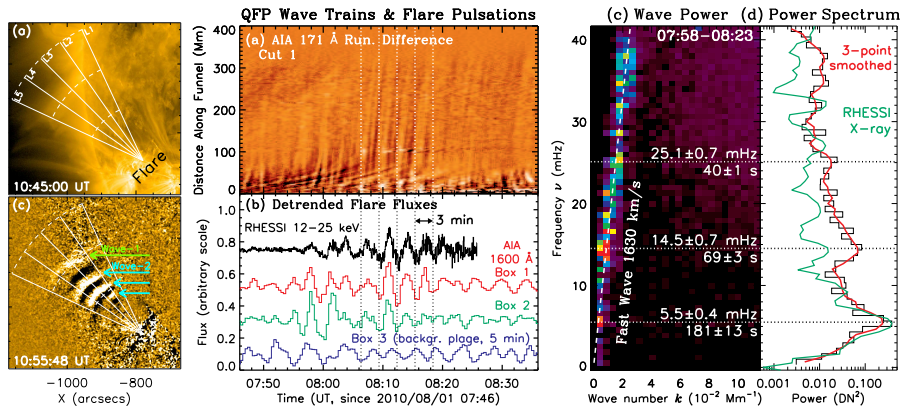

Figure 11. Examples of QFP wave trains observed by AIA and their frequency distributions. Left: Distinct QFP trains from a flare on 30 May 2011 shown in 171 Å running-difference (bottom) and direct (top) images (from Yuan *et al.*, 2013). Middle: QFP waves shown in a 171 Å space–time plot (top) and their correlated flare pulsations (bottom) displaying a dominant three-minute period. Right: Fourier power or k–ω diagram showing a bright ridge for the QFP waves and wave-number averaged power as a function of frequency on the right. The middle and right panels are from Liu *et al.* (2010) for the 01 August 2010 event.

To date, more than 15 QFP events have been identified in the AIA database, and far more may have been detected. A fraction of these events were analyzed in detail, whose characteristics are summarized in Table 5. Prior to AIA, periodic disturbances traveling at such high speeds and evidencing fast-magnetosonic wave trains were only imaged in a solar eclipse (Williams *et al.*, 2002) and in post-flare supra-arcades (Verwichte, Nakariakov, and Cooper, 2005). More common, non-imaging evidence was found in radio observations, such as decimetric bursts of $10 - 80$ second periods in a coronal fan above a null point (Mészárosová *et al.*, 2013) and fiber bursts of short $1 - 2$ second periods (Karlický, Mészárosová, and Jelínek, 2013).

Although at times QFPs can be identified at their source flares (Liu *et al.*, 2011), their initial appearances are often some distance away ($\gtrsim 100\,\mathrm{Mm}$). Such a distance is required for amplitude growth or a preferential LOS to be satisfied for detecting them (Cooper, Nakariakov, and Tsiklauri, 2003). In fact, their amplitudes usually increase with distance and then decrease, likely because of the interplay between amplification due to density stratification and attenuation due to geometric expansion of the funnel (Yuan *et al.*, 2013). QFPs often exhibit

Table 5. QFP wave trains observed in AIA's 171 Å channel.

Associated Flare			QFP Wave Characteristics				References
Date ddmmmyy	Start Time	GOES Class	Init. speed $[\mathrm{km\,s^{-1}}]$	Deceler. $[\mathrm{km\,s^{-2}}]$	Range [Mm]	Period Peaks [seconds]	
08Apr10	02:30	B3.8	$450-1200$	$0.2-5.8$	330	$40-240$	Liu *et al.* (2010)[1]
01Aug10	07:25	C3.2	2200		400	$40, 69, 181$	Liu *et al.* (2011)
08Sep10	23:00	C3.3	$1000-1200$	$3-4$	320	$30-240$	Liu *et al.* (2012)
25Mar11	23:08	M1.0	$1000-1300$		250	≈ 180	Kumar and Manoharan (2013)[2]
30May11	10:48	C2.8	830		220	$25-400$	Shen and Liu (2012b)
			$740-850$	$1.3-2.3$		$38, 40, 58$	Yuan *et al.* (2013)
23Apr12	17:38	C2.0	690	1.0	300	80	Shen *et al.* (2013a)
Typical Range		B–C	$500-2200$	$1-4$	$200-400$	$25-400$	Total: 6 events, 7 articles

[1]These results were not presented there, but QFPs are evident in their Figure 3h.
[2]Only two pulses were present and associated with an ejecta impact rather than a flare.

strong decelerations on the order of $1-4\,\mathrm{km\,s^{-2}}$, likely due to the decrease of the fast-magnetosonic speed with distance from the active region core. In an extreme case, they rapidly decelerate and terminate while approaching a CME front from behind, which was attributed to enhanced damping or dispersion in such a turbulent environment (Liu *et al.*, 2012). Expected dispersive evolution with decreasing periods was also identified (Yuan *et al.*, 2013). Many of these characters have been reproduced in MHD simulations (Ofman *et al.*, 2011; Pascoe, Nakariakov, and Kupriyanova, 2013).

QFPs often travel upward in *open funnels*, but occasionally in opposite directions along *closed loops* between conjugate flare ribbons (Liu *et al.*, 2011) and even two sympathetic flares across the Equator (Liu *et al.*, 2014a). These counter-propagating waves seem to be generated individually in association with their source flares, but it is possible that some of them are reflected repeatedly between the footpoints of closed loops.

4.2. Periodicities, Correlation with Flares, and Physical Origin

QFP waves are observed in a wide range of periods from 25 to ≈ 400 seconds, with the lower end limited by the Nyquist frequency of 42 mHz given by AIA's 12-second cadence. In Fourier power spectra or k–ω diagrams (*e.g.* Figure 11, right), QFPs appear as bright, nearly straight ridges passing through the origin, which describe their *dispersion relations* and indicate temporally averaged phase $[\nu/k]$ and group $[d\nu/dk]$ speeds indistinguishable given AIA's spatio–temporal resolution. Individual peaks of power on the ridge are often concentrated within a period range of $40-240$ seconds. Some QFP periods, *e.g.* two to three minutes or shorter, as shown in Figure 11 (middle), are correlated with *quasi-periodic pulsations* (QPPs) of accompanying flare emissions commonly seen from radio to hard X-rays (*e.g.* Fleishman, Bastian, and Gary, 2008; Inglis and Dennis, 2012; Dolla *et al.*, 2012; Su *et al.*, 2012). Such correlations suggest a common physical origin.

Proposed mechanisms for flare QPPs (see Nakariakov and Melnikov, 2009 for a review) fall into *two categories*: pulsed energy release intrinsic to magnetic reconnection and MHD oscillations, both relevant to the generation of QFP wave trains (Liu *et al.*, 2011; Shen *et al.*, 2013a). For example, oscillatory reconnection at X-type null points (McLaughlin *et al.*, 2012), repetitive generation and coalescence of plasmoids (Kliem, Karlický, and Benz, 2000) and their fast ejections (*e.g.* with a period of about two minutes, Liu, Chen, and Petrosian, 2013), or current sheet fluctuations induced by super-Alfvénic beams and associated Kelvin–Helmholtz instability nonlinear oscillations (Ofman and Sui, 2006) can cause *episodic energy release* in forms of plasma heating and particle acceleration that can result in emission pulsations and excite magnetosonic waves.

Meanwhile, *MHD oscillations* with periods determined by resonance or dispersion can modulate flare energy release or emission (Foullon *et al.*, 2005) and trigger magnetosonic waves. In particular, the strong three-minute QFP wave signal (see Figure 11, middle; Liu *et al.*, 2011) may be related to slow-mode magnetosonic waves leaking from the three-minute chromospheric sunspot oscillations (Jess *et al.*, 2012) that can trigger flare QPPs (Sych *et al.*, 2009). Long period ($\gtrsim 300$ seconds) QFP waves have been ascribed to the leakage into the corona of pressure-driven p-modes (Shen and Liu, 2012b). In this case, it implies that during QFP-associated eruptions, some yet to be determined special mechanisms or conditions (*e.g.* cone-shaped CME wakes seen in white-light eclipse images, Habbal *et al.*, 2011) must amplify these waves, which are otherwise expected to be seen anytime and anywhere on the Sun.

The funnel-shaped QFP paths often along large-scale coronal loops (open or closed) indicate the presence of *waveguides*, because in an otherwise homogeneous low-β plasma, fast-modes would propagate more isotropically both along and across magnetic-field lines like EIT waves. A waveguide can form in a channel of lower fast-magnetosonic speed [v_f], say, due to density enhancements, than the surrounding medium and thus trap waves by internal reflection. Another possibility is a leaky waveguide where a high v_f region is surrounded by a low v_f background (*e.g.* Ofman and Davila, 1995). Such waveguides of finite widths results in dispersion with components of different frequencies propagating at different speeds. This can produce additional periods (Pascoe, Nakariakov, and Kupriyanova, 2013), independent of a periodic driver. An impulsively generated fast-mode wave can dispersively evolve into a quasi-periodic wave train (Roberts, Edwin, and Benz, 1984), as manifested in AIA detection of distinct wave trains each associated with a radio-burst episode (Yuan *et al.*, 2013).

4.3. Wave Trains Inside and Outside CME Bubbles

QFPs in coronal funnels are apparently different from quasi-periodic wave trains within broad EIT wave pulses (see Section 3.3) in temperature, speed, and spatial domain with respect to CMEs. As shown in Figure 12, QFPs are best (and often only) seen at 171 Å (suggestive of lower temperatures) within CME bubbles, while EIT wave trains are most evident at 193 and 211 Å ahead of CME flanks. When these wave trains are both detected in the same event off the limb (Liu *et al.*, 2012; Liu *et al.*, 2014b) or possibly on the disk (Liu *et al.*,

2010; Shen and Liu, 2012b; Shen *et al.*, 2013a), the funnel QFPs are usually
two to three times faster than their EIT wave counterparts. This is consistent
with the rapid decrease of the fast-magnetosonic speed away from active regions.
Another possible contribution to the higher speeds of QFPs is the faster fall-off
of density with height due to gravitational stratification of the cooler 171 Å
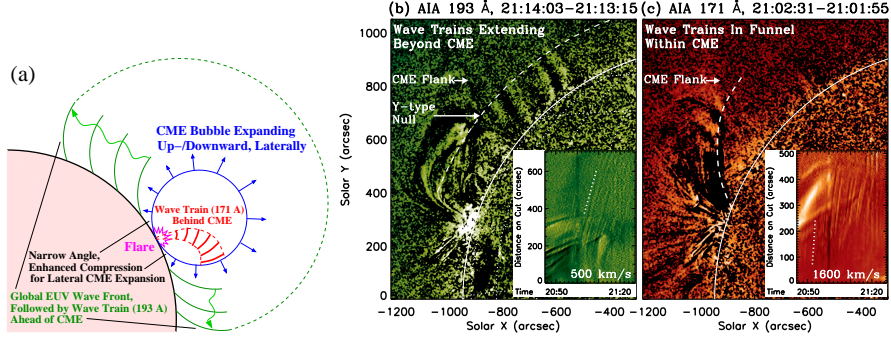emitting plasma and thus higher Alfvén speeds (Ofman *et al.*, 2011).

Figure 12. (a) Schematic of quasi-periodic wave trains outside (green) and inside (red) a
CME bubble (blue) (from Liu *et al.*, 2012). The former propagates along the solar surface
and follows the leading front of the broad EIT wave pulse that is driven by the lateral and
downward CME expansions initiated at an elevated height. The narrow angle formed between
the CME bubble and the underlying chromosphere can cause enhanced compression due to the
lateral CME expansion (see Section 3.10). The QFP wave trains behind the CME originate at
the flare and propagate along a narrow funnel. (b) and (c) Example of two wave trains in the
same event that appear in running-difference AIA images preferentially outside (193 Å, green)
and inside (171 Å, red) the CME (from Liu *et al.*, 2014b). The insets are space–time plots
obtained from cuts indicated by the white dashed lines in the images. The wave trains exhibit
as zebra-like steep stripes at typical speeds of 500 and 1600 km s^{-1}. Note in (b) an abrupt
change in wave speed at the CME flank shown as the outermost shallow stripe near $s = 350''$.

Aside from their differences, such wave trains sometimes have considerable
spatial overlap (*e.g.* Shen *et al.*, 2013a) and even share some similar periods with
the accompanying flare pulsations (Liu *et al.*, 2012). EIT wave trains detected
thus far are always accompanied by funnel QFPs, but not *vice versa*. In off-limb
events the QFP funnel at times gradually turns from vertical to horizontal, and
the EIT wave trains travel horizontally along the solar surface.

Because of these similarities, we posit that that EIT wave trains beyond
CME bubbles are the *continuation* of QFP wave trains within funnels. In other
words, both types of wave trains can share the same excitation agent but exhibit
different propagation behaviors, such as temperatures, speeds, and periods or
wavelengths, determined or modified by their respective media, for example,
due to dispersion. This continuation can happen under favorable conditions,
e.g. when a funnel waveguide turns horizontal with distance or when QFPs are
refracted back toward the solar surface. Such conditions, somewhat stringent,
may explain the relative infrequency of EIT wave trains compared with funnel
QFPs. In fact, the increase of Alfvén speed with height on the quiet Sun due to
the faster fall-off of density than magnetic field can create a horizontal waveguide
aligned above the solar surface (*e.g.* Afanasyev and Uralov, 2011; Kwon *et al.*,

2013a). This waveguide can form an extension of an asymptotically horizontal funnel, confine EIT wave trains to their observed heights $\lesssim 100$ Mm or one to two density scale heights, and produce their forward inclinations (*cf.* Liu *et al.*, 2012). As QFPs evolve into EIT wave trains on the quiet Sun, abrupt changes in speed can occur at topological interfaces or CME flanks between media of different fast-magnetosonic speeds (*e.g.* Figures 12b and 12c; Shen *et al.*, 2013a).

Another possible origin of EIT wave trains is *leakage* from funnel waveguides, which can happen for sausage modes, for example, with wavelengths greater than the cutoff value and incident angles at the funnel boundary being smaller than the total internal reflection angle (Pascoe, Nakariakov, and Kupriyanova, 2013). These possibilities remain to be validated with more detailed observations and more sophisticated MHD models.

5. Small-scale EUV Waves and Wave-like Phenomena

In addition to large-scale waves, AIA has observed various small-scale waves, including mini-EUV waves and nonlinear waves or vortices associated with magnetic Kelvin–Helmholtz instabilities, which add to the multitude of EUV wave and wave-like phenomena. An exhaustive list of such events detected by AIA and their characteristics are given in Table 6.

5.1. Mini-EUV Waves

Mini-EUV waves associated with small-scale eruptions are miniature versions of EIT waves. They were first detected by STEREO/EUVI (Innes *et al.*, 2009; Podladchikova *et al.*, 2010) and then commonly seen by SDO/AIA (Zhang and Liu, 2011; Zheng *et al.*, 2011, 2012b, 2012c, 2012d, 2013a). They share similar characteristics with EIT waves, including quasi-circular shapes, often uniform speeds sometimes with decelerations, instigating loop oscillations, being driven or triggered by energy release events such as mini-CMEs and micro-flares, as well as spatial-decoupling from their drivers. The key difference between EIT waves and mini-EUV waves is their *distinct source regions* that define their energy budgets and physical characters. Global EIT waves are associated with release of large amounts of free energy on the order of 10^{32} erg via CMEs or flares in *active regions*. Mini-EUV waves originate *away from active regions* with orders of magnitude less free energy available, giving rise to their somewhat smaller ranges of $20 - 400$ Mm, shorter lifetimes of $10 - 30$ minutes, and weaker wave intensities and dimmings.

Accompanying a variety of small-scale eruptions, including mini-CMEs, micro-flares, mini-filament and micro-sigmoid eruptions, jets, and surges, mini-EUV waves fall into two categories (see Table 6): i) Those from *ephemeral regions* involving flux emergence or cancellation tend to be larger in size and faster at typically $200 - 500$ km s^{-1}, and are thus interpreted as fast-mode waves (*e.g.* Zheng *et al.*, 2011). They closely resemble EIT waves and hence we call them "mini-EIT waves". ii) Those from the *quiet Sun*, for example, triggered by supergranular flows (Innes *et al.*, 2009) or by coronal cyclones associated with

Table 6. AIA observed small-scale EUV waves.

(1) mini-EUV waves						
Date ddmmmyy	Start Time	Duration [minutes]	Speed[1] [km s^{-1}]	Range [Mm]	Associated Phenomena	References
(1.1) Ephemeral-region mini EIT waves						
21Oct10	20:37	13	$270-350$	250	micro-sigmoid/B1.7 flare	Zheng *et al.* (2012c)
11Nov10	18:10	$10-20$	$280-500$	360	surge-driven, homologous	Zheng *et al.* (2012d)
01Dec10	02:54	17	$220-250$	180	mini-CME	Zheng *et al.* (2011)
01Mar11	13:00	13	$260-350$	260	failed filament eruption	Zheng *et al.* (2012b)
04Oct12	06:16	12	$300-360$	300	micro-sigmoid/CME/flare	Zheng *et al.* (2013a)
Typical Range		10-20	$200-500$	180-360		Total: 5 events
(1.2) Quiet-Sun mini-EUV waves						
20Jul10	11:00	8	$35-85$	20	quiet-Sun cyclones	Zhang and Liu (2011)

(2) Kelvin–Helmholtz instability vortices associated with CMEs/ejecta					
Date ddmmmyy	Start Time	GOES Class	Speed[2] [km s^{-1}]	λ [Mm]	References
08Apr10	02:30	B3.7	$6-14$	≤ 7	Ofman and Thompson (2011)
03Nov10	12:07	C4.9	420	18	Foullon *et al.* (2011, 2013); Bain *et al.* (2012)[3]
24Feb11	07:23	M3.5	310	14	Möstl, Temmer, and Veronig (2013)
Typical Range		$B-M$	$10-400$	$7-18$	Total: 3 events

[1]Initial or average speed.
[2]Phase speed.
[3]On the associated Type-II burst and AIA observations of the plasmoid ejection.

rotating network magnetic fields (Zhang and Liu, 2011), tend to be smaller and slower at typically $10-100\,\mathrm{km\,s^{-1}}$, and thus possibly evidence slow-mode waves (Podladchikova *et al.*, 2010) or non-wave coronal reconfigurations. Innes *et al.* (2009) estimated that quiet-Sun mini-eruptions can be numerous at a high rate of 1400 per day, with one third producing mini-EUV waves. Considering the ensemble of EUV waves of such hierarchic sizes and speeds (Patsourakos and Vourlidas, 2012), mini-EUV waves can constitute an extension of the size distribution of large-scale EIT waves, like the extension of their drivers, *i.e.* CMEs, toward smaller scales (Schrijver, 2010; Innes and Teriaca, 2013), which involve (impulsive) mass motions of some kind.

5.2. Magnetic Kelvin–Helmholtz Instability Waves

Another serendipitous discovery of AIA was the detection of Kelvin–Helmholtz Instabilities (KHIs) in the magnetized corona, which can play important roles in mass and energy transfer during solar eruptions (Ofman and Thompson, 2010, 2011; Foullon *et al.*, 2011, 2013; Möstl, Temmer, and Veronig, 2013). Observed at
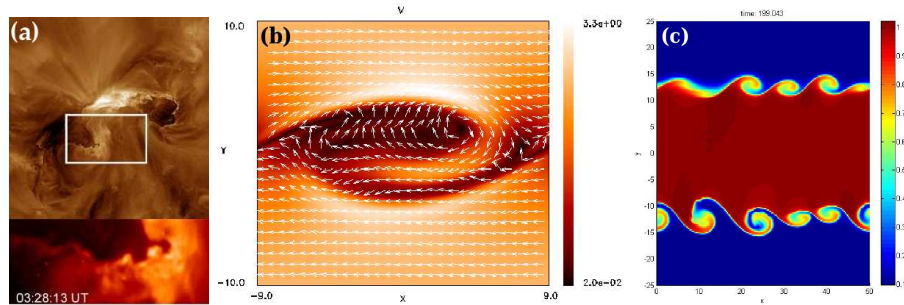
Figure 13. Small-scale, nonlinear waves associated with magnetic Kelvin–Helmholtz instabilities observed by AIA on 08 April 2010 at 193 Å (a) and simulated plasma velocity (b) (both from Ofman and Thompson, 2011). (c) Simulated plasma density for the KHI event associated with the 24 February 2011 M3.5 flare (from Möstl, Temmer, and Veronig, 2013).

velocity-shear boundaries, *e.g.* flanks of high-speed CMEs or ejecta, KHIs appear as a series of vortices of wavelengths on the order of 10 Mm traveling along the boundaries at phase speeds of $10 - 400 \, \mathrm{km \, s^{-1}}$ (see Figure 13a and Table 6). KHIs were also detected in prominences (Berger *et al.*, 2010; Ryutova *et al.*, 2010) and high-corona streamers (Feng, Inhester, and Gan, 2013). Numerical models (*e.g.* Figures 13b and 13c) played a crucial role in identifying KHIs by comparing observations with simulated formation and growth of the associated nonlinear waves (Ofman and Thompson, 2011; Soler *et al.*, 2012; Möstl, Temmer, and Veronig, 2013; Nykyri and Foullon, 2013; Zaqarashvili, Vörös, and Zhelyazkov, 2014). Such models also allow seismological inference of the strengths and relative orientations of the magnetic fields across the velocity shear boundary.

6. Coronal Seismology Using EUV Waves

Like any propagating disturbances, EUV waves can provide potential diagnostics for their medium, *i.e.* the (large-scale) solar corona (Ballai, 2007; Ballai and Douglas, 2008). Compared with the rapid development of local coronal seismology using loop oscillations in the last two decades (Nakariakov and Verwichte, 2005), advances in global coronal seismology using large-scale EUV waves have been hindered mainly because of the long debate on the nature of EIT waves. Now that this controversy is coming to an end and it is clear that at least their leading fronts are true fast-mode waves, global seismology is becoming a reality. We summarize below recent advances in this area using EIT waves and QFP wave trains to infer the *magnetic, thermal, and energy* properties of the corona. Note that because of the density stratification and the $\propto n^2$ dependence of EUV emission, EUV wave seismology is usually limited to the inner corona, *e.g.* up to heights of $\approx 100 - 200$ Mm. Seismology in the outer corona resorts to alternative observables, such as white-light streamer waves (Chen *et al.*, 2011b; Feng *et al.*, 2011) and quasi-periodic radio bursts (Zaqarashvili *et al.*, 2013).

6.1. Magneto-Seismology

Inferring the elusive coronal magnetic field is one of the primary goals of coronal seismology, which complements other approaches including polarimetric measurements using Zeeman and Hanle effects (Lin, Penn, and Tomczyk, 2000), extrapolations of surface magnetograms (Zhao and Hoeksema, 1994; De Rosa *et al.*, 2009), and radio observations of gyro-resonance emission (Gary and Hurford, 1994; White and Kundu, 1997). The fast-magnetosonic speed weakly depends on the direction of the wave vector with respect to the magnetic field, which has a strong vertical component in the quiet Sun and is thus practically assumed to be perpendicular to the predominantly horizontal EIT wave vectors. The fast-magnetosonic speed therefore reduces to a simple form

$$v_{\mathrm{f}} = \sqrt{v_{\mathrm{A}}^2 + c_{\mathrm{s}}^2}, \tag{1}$$

where $v_{\mathrm{A}} = B/\sqrt{4\pi\rho}$ is the Alfvén speed, which depends on the magnetic-field strength $[B]$ and mass density $[\rho]$, and $c_{\mathrm{s}} \propto \sqrt{T}$ is the sound speed, which depends on the temperature $[T]$. A single temperature is usually assumed for simplicity, although the corona is multithermal. With the knowledge of v_{f}, T, and ρ, the magnetic-field strength can be calculated in cgs units as

$$B = \sqrt{4\pi\rho(v_{\mathrm{f}}^2 - c_{\mathrm{s}}^2(T))}. \tag{2}$$

For EIT waves that are *linear fast magnetosonic*, one can equate their measured speeds and v_{f} with uncertainties subject to projection effects among others. In the quiet-Sun corona, the temperature is on the order of $1-2$ MK giving $c_{\mathrm{s}} = 150-210 \, \mathrm{km \, s^{-1}}$. Density measurements are more challenging because of LOS integration and unknown filling factors. Fortunately, the uncertainty in magnetic field due to density is small because of the $\sqrt{\rho}$ dependence (*e.g.* Nakariakov and Ofman, 2001). Early studies used *atmosphere models* to estimate the density (Warmuth and Mann, 2005; Ballai, 2007). More accurate estimates were made with *density-sensitive line ratios*, such as Si X 258 Å/261 Å, from spectroscopic measurements. Applying this to *Hinode*/EIS data, West *et al.* (2011) inferred a weak quiet-Sun magnetic field of $\approx 1 \, \mathrm{G}$ in 2009 during the deep solar minimum, while Long *et al.* (2013) found $2-6$ G at heights of $70-130$ Mm in $2010-2011$ during the rise phase of this solar cycle. Alternatively, using *tomographic density reconstruction* (Kramar *et al.*, 2009), Kwon *et al.* (2013b, 2013a) found fields of $0.4-2.5$ G at heliocentric distances of $1-3 \, \mathrm{R_{\odot}}$ in the extended corona (see Figure 14, left) and higher field strengths and plasma β in streamers than in coronal holes.

For *fast-mode shock* cases, v_{f} can be obtained from the measured EIT wave speed $[v_{\mathrm{EIT}}]$ and the fast-mode Mach number $[M_{\mathrm{f}} = v_{\mathrm{EIT}}/v_{\mathrm{f}}]$ ($\approx$ the Alfvén Mach number $[M_{\mathrm{A}}]$ for low-β plasmas) inferred from the Rankine–Hugoniot jump condition given the *compression ratio* $[n/n_0]$. The latter can be estimated with *Type-II burst band-splitting* $[n/n_0 = (f_{\mathrm{U}}/f_{\mathrm{L}})^2]$ where f_{U} and f_{L} are the upper and lower branch frequencies, respectively (*e.g.* Ma *et al.*, 2011; Kouloumvakos *et al.*, 2014), or with the *EUV intensity ratio* $[n/n_0 = \sqrt{I/I_0}]$ by ignoring
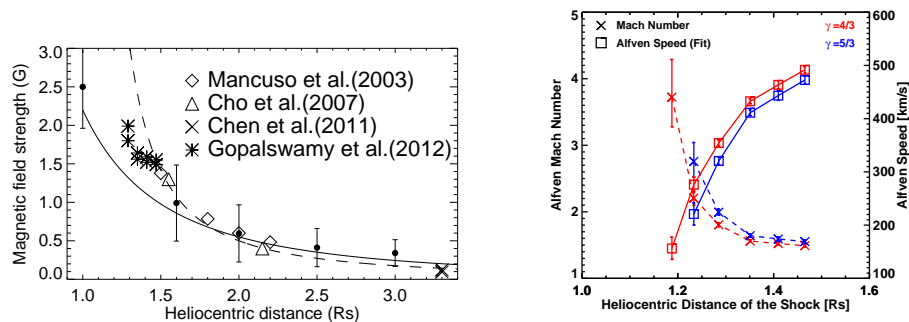
Figure 14. Examples of coronal-seismology results. Left: magnetic-field strength inferred from the lateral propagation speed of a coronal wave on 04 August 2011 as a function of heliocentric distance (from Kwon *et al.*, 2013b). Right: Height distribution of the derived Alfvén speed and Mach number from the 13 June 2010 EIT wave and shock (from Gopalswamy *et al.*, 2012).

heating and thus obtaining upper limits (Veronig *et al.*, 2010; Kienreich *et al.*, 2011; Muhr *et al.*, 2011; Shen and Liu, 2012a). Such estimates have yielded n/n_0 and M_f values of $1-1.5$ and magnetic fields of $1.5-3.5$ G. Alternatively, Gopalswamy *et al.* (2012) obtained the Mach number (see Figure 14, right) from the *shock-standoff distance* and the curvature radius of the shock-driving flux rope, and the density from the Type-II burst frequency according to an atmosphere model. They obtained magnetic fields of $1.3-1.5$ G at heliocentric distances of $1.2-1.5\,R_\odot$.

For coronal funnels rooted in active regions in which QFP wave trains are observed to propagate, their typical speed is $1000\,\mathrm{km\,s^{-1}} \gg c_s$, and thus $v_f \approx v_A$ and $B \approx v_f\sqrt{4\pi\rho}$. For QFPs in the linear fast-mode regime, AIA passband responses were used to estimate lower limits of ρ and thus lower limits of B in the range of $2-8$ G (Liu *et al.*, 2011; Shen and Liu, 2012b; Shen *et al.*, 2013a).

6.2. Thermal-Seismology

Thermal-seismology with EUV waves, proposed by Downs *et al.* (2012), is a relatively new approach to probe the thermal properties of the local corona. The temperature distribution or differential emission measure (DEM) of the coronal plasma has been traditionally inferred from *snapshots* of multiple EUV passband data using forward modeling (*e.g.* Aschwanden *et al.*, 2013) or inversion (*e.g.* Weber *et al.*, 2004; Schmelz *et al.*, 2011), each with its own advantages and disadvantages (Guennou *et al.*, 2012a; 2012b). Large-scale EUV waves, by perturbing the corona and producing *temporal* variations, can provide additional constraints not only on the wave itself but also on its medium.

For example, as discussed in Section 3.8, the general trend of 193/211 Å brightening and 171 Å darkening at EIT wave fronts indicates heating of the perturbed corona from an initial temperature range of $0.8-1.6$ MK determined by the peak responses of these channels, while the exception of 193 Å darkening in some cases indicates higher initial temperatures $\gtrsim 1.6$ MK. The temperature

resolution of all AIA passbands combined is estimated at $0.03 \log T$ (Guennou *et al.*, 2012a). Such a sensitivity is manifested in those so-called tri-color composite emission maps (see Figures 2 and 8, right), which show that as little as a $0.3\,\%$ temperature rise with or without adiabatic compression can account for typical EUV intensity changes of a few percent (Downs *et al.*, 2012).

Note that, because of their sensitive dependence on local plasma and magnetic conditions, any change in time or space of kinematic or thermal properties of EUV waves serves as a probe to the temporal evolution or spatial inhomogeneity of the large-scale corona. For example, wave reflections or abrupt speed changes indicate interfaces between drastically different plasmas or magnetic fields. Such a potential using large-scale EUV waves in magneto–thermal seismology is yet to be exploited.

6.3. Energy-Seismology

Aside from local coronal seismology applications, forced transverse oscillations discussed in Section 3.6, with their kinetic energies, can be used to estimate the energy contents of their triggering agents, *i.e.* EIT waves. The estimate depends on proper evaluation of the coupling between the EIT wave and the oscillating loop, and the fractional reflection, trapping, and transmission of the wave energy, *e.g.* by using realistic MHD models of such events (*e.g.* Ofman, 2007; Downs *et al.*, 2012). Such estimates were obtained at $10^{23} - 10^{26}$ erg as lower limits from loop oscillations (Ballai, Erdélyi, and Pintér, 2005; Ballai, 2007) and at 10^{28} erg from oscillations of a flux-rope coronal cavity (Liu *et al.*, 2012). The latter is close to a more complete estimate of 10^{29} erg by including kinetic, radiative loss, and conductive energies (Patsourakos and Vourlidas, 2012), and comparable to the typical energy of 10^{28} erg of a micro-flare (Hannah *et al.*, 2008).

For QFP waves, one can assume the observed EUV intensity variations due to density perturbations alone, which is reasonable because unlike EIT waves, QFPs analyzed so far show no sign of heating or cooling. The kinetic energy of the perturbed plasma can thus be obtained and used as a lower limit to estimate the wave-energy flux which was found in the range of $(0.1 - 2.6) \times 10^5 \, \mathrm{erg\, cm^{-2}\, s^{-1}}$ (Liu *et al.*, 2011; Shen *et al.*, 2013a). Such fluxes are sufficient for *coronal heating* in active regions (Withbroe and Noyes, 1977), although the overall contribution by QFPs could be small due to their low occurrence rate (only during flares/CMEs).

7. Methodologies for EUV Wave Research

Methodologies adopted in EUV wave research have direct impact on our capabilities to achieve the best science from observations and to probe their underlying physics. To this end, advanced data-analysis techniques and numerical or analytical models have played important roles in recent years.

7.1. Data Analysis Techniques

A key task for EUV wave research is to identify the wave front and track it in space and time. Many early studies were based on observer's visual identification in running- or base-difference images and on point-and-click measurements, which introduce an element of subjective interpretation of the data. The immense data volume with the advent of SDO/AIA made this traditional technique impractically labor intensive and necessitated *automatic wave detection*. The first two such algorithms were i) the Novel EIT wave Machine Observing (NEMO: Podladchikova and Berghmans, 2005) package utilizing image profiles, recently updated with a clustering technique for dimming extraction (Podladchikova *et al.*, 2012), and ii) the mapping technique of Wills-Davey (2006), using the Huygens principle to track wave trajectories.
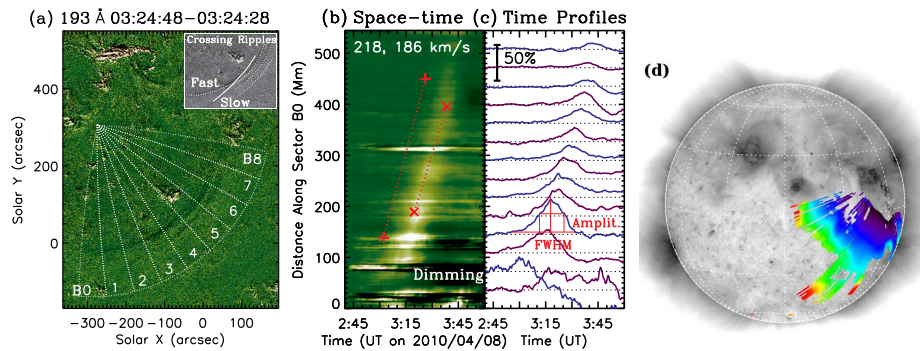
Figure 15. Examples of EIT wave analysis techniques. (a) Spherical sectors overlaid on a running-difference image of the 08 April 2010 EIT wave for obtaining (b) a base-difference space–time plot and (c) intensity profiles at fixed locations, from which pulse amplitude, FWHM, and onset and peak positions/speeds can be measured (from Liu *et al.*, 2010). (d) Wave ground tracks identified by the CorPITA algorithm (Long *et al.*, 2014) with colors from black to red indicating time elapsed in 20 minutes (from Byrne *et al.*, 2013).

As the cornerstone of various recently developed algorithms (*e.g.* Veronig *et al.*, 2010), NEMO projects EUV images onto the solar surface and obtains intensity profiles along spherical sectors originating from the epicenter (*e.g.* Figure 15, left), thus recovering "ground tracks" of EIT waves. Next, a common practice is to compose such 1D profiles at different times into a 2D space–time diagram or stack plot (Figure 15, middle), from which wave properties such as front kinematics and pulse amplitudes and widths can be retrieved automatically (*e.g.* Liu *et al.*, 2010) or by repeated visual measurements. A similar approach adopted in the Coronal Pulse Identification and Tracking Algorithm (CorPITA; Long *et al.*, 2014; Figure 15, right), which has been implemented in the SDO computer vision project (Martens *et al.*, 2012), involves fitting 1D profiles with a Gaussian to characterize kinematics and wave dispersion. Derivatives of these approaches employ cuts in various geometries to accommodate specific situations, such as cuts at constant heights above the limb to track off-limb waves. Recently, Byrne *et al.* (2013) adopted robust statistical techniques to remedy

undesired numerical effects arising from deriving EUV wave kinematics from scattered space–time data.

The above ground-track techniques neglect heights of EIT waves by assuming that all emission originates from the spherical solar surface. Near disk center, this inconsistency causes only a negligibly small error in travel distance at a constant height, *e.g.* $\lesssim 1\,\%$ for $h = 100\,\mathrm{Mm}$. Near the limb, however, any change in height (*e.g.* vertical propagation) can result in significant overestimates of velocities projected onto the spherical surface, as demonstrated in 3D MHD simulations (Hoilijoki *et al.*, 2013). 3D reconstruction of EIT waves from STEREO observations has been recently attempted with triangulation techniques (Delannée *et al.*, 2014). In doing so, extra care must be taken to account for optically thin EUV wave emission, whose integration along different lines of sight never corresponds to the same feature, unlike optically thick emission (*e.g* some line emission from prominences).

For tracking waves and oscillations in general, a range of algorithms were or are currently being developed, such as a coherence/travel-time based approach (McIntosh, de Pontieu, and Tomczyk, 2008), an interactive web system (Sych *et al.*, 2010), a Bayesian-based approach (Ireland *et al.*, 2010), phase-speed measurements with various fitting techniques (Yuan and Nakariakov, 2012), and EIT wave detection using advanced image processing and the SunPy python library (Ireland *et al.*, 2012).

Fourier analysis of wave power and dispersion relation with k–ω diagrams is a common technique in helioseismology, but was previously underused in coronal seismology mainly because of the scarcity of high-cadence data (DeForest, 2004; Tomczyk and McIntosh, 2009). AIA filled this gap and offered a new venue for this technique, which has been widely used for analysis of QFP wave trains as noted earlier (Liu *et al.*, 2011; Shen and Liu, 2012b).

7.2. Numerical and Analytical Models

Recent modeling efforts pertinent to large-scale EUV waves fall into two categories: 2D/3D MHD simulations for EIT waves and QFP wave trains and analytical or numerical models for shock formation and propagation.

Early 2D MHD models of EIT waves in Cartesian geometries, although simple, were able to capture some essential features, such as the bimodal composition of a fast-mode (shock) wave ahead of a CME driven compression (Chen *et al.*, 2002; Chen, Fang, and Shibata, 2005; Pomoell, Vainio, and Kissmann, 2008). More recent 2D models revealed the presence of a fast-mode shock and its reflection from the chromosphere together with a slow-mode shock and velocity vortices surrounding a CME (Wang, Shen, and Lin, 2009; Mei, Ziegler, and Lin, 2012).

3D MHD models capture some crucial physics missing in 2D models that assume an invariant third dimension. For example, the linear and nonlinear coupling between the fast mode and other MHD modes in inhomogeneous plasma requires 3D modeling. 3D models in Cartesian geometries focus on *local* behaviors of EUV waves, such as reflections or transmissions and flare-triggered loop oscillations in bipolar active regions (Ofman and Thompson, 2002; Ofman, 2007), non-wave current shells surrounding CMEs (Delannée *et al.*, 2008; Schrijver

et al., 2011), and dome-shaped EIT waves from rotating active regions (Selwa, Poedts, and DeVore, 2012, 2013). Recently, Hoilijoki *et al.* (2013) demonstrated that, because of LOS integration, observed EIT wave speeds are highly dependent on viewing angles and can vary by nearly a factor of two. 3D models in spherical geometries using more realistic magnetic fields from extrapolations of magnetograms allow for tracking *global* propagation of EIT waves. For example, Wu *et al.* (2001) found that a fast-mode wave in a coronal region of $\beta \approx 1$ can explain an observed EIT wave. Using the coronal module of the Block-Adaptive Tree Solar-wind Roe Upwind Scheme (BATSRUS) code (Roussev *et al.*, 2003), Cohen *et al.* (2009) confirmed the wave/non-wave bimodality, and Schmidt and Ofman (2010) reproduced the observed EIT wave reflection from a coronal hole.
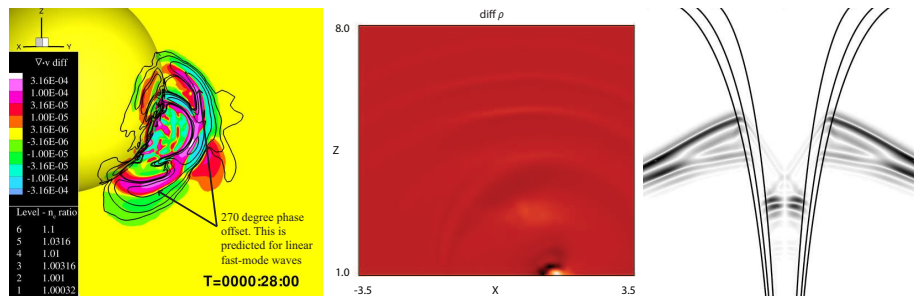
Figure 16. Examples of numerical simulations for EUV waves. Left: Divergence of perturbed velocity in color showing a sign reversal from negative to positive (green to pink; *i.e.* from compression to expansion) that coincides with the maximum density enhancement (black contours), as expected for a compressible fast-mode wave component of an EIT wave (from Downs *et al.*, 2011). Middle: Density perturbations of a modeled QFP train (from Ofman *et al.*, 2011). Right: Simulated velocity perturbations for confined and leaked "wing" QFP waves from a funnel-shaped waveguide (from Pascoe, Nakariakov, and Kupriyanova, 2013).

A recent advance in 3D global MHD models is to *synthesize EUV emission* by convolving simulated density and temperature distributions with instrument response functions (Downs *et al.*, 2011, 2012), as previously done for 2D models (Chen, Ding, and Fang, 2005). This allows for direct comparison with observables, *e.g.* from EUVI or AIA, to constrain the models and perform thermalseismology. Downs *et al.* (2012) established a unified picture supporting the hybrid wave/non-wave model of EIT waves. Specifically, as shown in Figure 16 (left), they found through phase analysis that the highest density enhancement is cospatial with the maximum compression located in the outer EUV front, as expected for a compressible fast-mode wave. However, the bulk CME motion and an associated current shell and reconnection front are located further inside, as part of the non-wave, inner EUV component.

QFP wave trains were modeled as fast-mode magnetosonic waves with a 3D MHD code in a Cartesian geometry (Ofman *et al.*, 2011). They are excited by periodic velocity pulsations at one pole of a bipolar active region and produce density fluctuations by compressibility (see Figure 16, middle) that match the observed QFP signatures (Liu *et al.*, 2011), including reflections within closed loops. A funnel-shaped *leaky waveguide* is achieved by the fast-magnetosonic speed distribution determined by the diverging magnetic field and

density stratification. A similar waveguide formed with density enhancement within a funnel was constructed with a 2D MHD model by Pascoe, Nakariakov, and Kupriyanova (2013). They reproduced observed QFP amplitude growth and deceleration (Yuan *et al.*, 2013) and found additional "wing" wave trains leaking from the funnel (see Figure 16, right).

Shock formation and propagation have been extensively investigated both analytically and numerically (see Vršnak and Cliver, 2008 for a review), which is relevant to a subset of strong EIT waves that are shocked. Analytical solutions were obtained for piston-driven shock formation in 1D planar geometries (Mann, 1995; Vršnak and Lulić, 2000), in 2D cylindrical and 3D spherical geometries (Žic *et al.*, 2008), and applied to an expanding sphere with a rising center in comparison with Moreton-wave observations (Temmer *et al.*, 2009). A recent development involved 2.5D MHD simulations of shock formation driven by a cylindrical piston (Lulić *et al.*, 2013). A general conclusion is the positive dependence of the (shock) wave amplitude and phase speed on the *acceleration of the piston*. This bears strong implications for the early (lateral) CME expansion discussed in Section 3.10.

Another line of research focuses on the propagation of a shock or linear MHD wave after its generation. The pioneering work of Uchida (1968, 1974) applied *linear geometric acoustics* or ray tracing with the Wentzel–Kramers–Brillouin (WKB) approximation to follow fast-mode (weak shock) wave propagation governed by the spatial (height) distribution of the fast-magnetosonic speed and to explain Moreton waves and Type-II bursts. The same approach was adopted in the modern observational context of EIT waves (Wang, 2000; Patsourakos *et al.*, 2009). Recently, *nonlinear* effects such as energy dissipation and the dependence of wave speed on amplitude were included (Afanasyev and Uralov, 2011; Afanasyev, Uralov, and Grechnev, 2013). The results were applied to a coherent picture unifying observations of EIT waves, Type-II bursts, and CMEs (Grechnev *et al.*, 2011a, 2011b).

8. Conclusions and Prospects

We have presented a review of recent advances in EUV wave research focusing on new observations since the launch of SDO and related data-analysis techniques and models. Thanks to its advanced capabilities, SDO/AIA not only played a critical role in ending the 15-year-long debate on the nature of EIT waves, allowing them to be used for coronal seismology, but also opened new research areas for newly discovered coronal phenomena, such as QFP wave trains and magnetic KH instabilities with associated nonlinear waves. We summarize below the current status and future prospects of these topics.

Backed up with strong observational and numerical evidence, the *hybrid or bimodal nature of EIT waves* has been established. In this general picture, an outer EUV front of a true fast-mode (shock) wave travels ahead of an inner non-wave component of CME-driven compression. Heating due to electric current dissipation or magnetic reconnection may contribute to the EUV emission at the inner, CME front, but not the outer, true wave front. AIA revealed an

average EIT wave speed $> 600\,\mathrm{km\,s^{-1}}$ that is well expected for coronal fast-mode waves but much higher than the typical speeds of $200-400\,\mathrm{km\,s^{-1}}$ from previous SOHO/EIT measurements. A wide range of behaviors intrinsic to fast-mode waves are now commonly observed, including quasi-periodic wave trains, reflections and transmissions, coherent periodicities, sequential structural oscillations, and heating-cooling cycles. The impulsive lateral and downward expansions of a CME are believed to be key in generating EIT waves (see Section 3). Outstanding questions regarding EIT waves include:

i) quantitative relation between their generation and CME (lateral) expansion;
ii) their roles in transporting energy and triggering sympathetic eruptions;
iii) their physical relation with Type-II bursts, Moreton waves, and SEPs.

As one of AIA's discoveries, QFP wave trains with typical speeds of $500-2200\,\mathrm{km\,s^{-1}}$ are evidence of fast-mode magnetosonic waves in funnel-shaped waveguides from active regions. They are commonly associated with quasi-periodic flare pulsations (Section 4). Open questions on QFPs include:

i) the origin of periodicities, especially those not identified in flare pulsations with possible connections to three-minute sunspot and other (sub)surface oscillations;
ii) their roles in energy transport and coronal heating;
iii) the relation between QFPs within funnels and quasi-periodic wave trains within EIT waves ahead of CME flanks.

Small-scale EUV waves including mini-EUV waves and KHI waves are relatively new and require further investigation to fully uncover the statistical distributions of their physical parameters. Mini-EUV waves are less energetic but more numerous than their large-scale counterparts (Section 5). Thus their total energy budget could be significant for the quiet Sun. As for nano- or micro-flares in the flare size distribution, mini-EUV waves may play an important role in the full spectrum of EUV waves of hierarchic sizes. Such possibilities could be topics of future research.

Seismological practice using EIT waves and QFPs to probe the coronal magnetic fields and thermal states and wave-energy fluxes is being actively pursued. The currently inferred quiet-Sun magnetic fields are in the range of $1-10$ G with uncertainties of about the same order (Section 6). Improving this accuracy, *e.g.* with refined density and temperature estimates, will be a critical future task. There are other potential diagnostic techniques to be explored, *e.g.* by including mini-EUV waves and using wave reflections and transmissions to probe topological interfaces.

A whole suite of data-analysis techniques is becoming mature and has started to produce fruitful results (Section 7.1). However, automatic detection and tracking of EUV waves have not been widely tested or used. Their performance in data-processing pipelines remains to be seen and will be critical to fully explore rich observations offered by AIA and other instruments. We emphasize that detailed analysis of individual well-observed events and statistical analysis of large samples are equally important.

Numerical models are crucial in lending credence to data interpretation and in understanding the underlying physics. Particularly useful are those 3D MHD models with realistic initial and boundary conditions that can produce synthesized observables to be directly compared with observations (Section 7.2).

In the years to come, the diagnostic power enabled by AIA's spatio–temporal and thermal coverage remains to be fully exploited to answer the above open questions about coronal EUV waves. The future EUV imager and spectrometer onboard the *Solar Orbiter* mission, scheduled for launch in 2017, and the EIS counterpart onboard the currently planned *Solar-C* mission will likely make further contributions. Additional constraints can be obtained from complementary observations of the solar atmosphere beyond the corona or at wavelengths outside the EUV regime. The *Interface Region Imaging Spectrograph* (IRIS: De Pontieu *et al.*, 2014), launched in June 2013, can detect potential UV signatures of coronal waves and Moreton waves in the transition region and chromosphere, such as Doppler, density, and temperature perturbations, and help identify the origin of QFP wave periodicities in regard to flares and chromospheric oscillations. The ground-based *Daniel K. Inouye Solar Telescope* (DKIST), previously known as the *Advanced Technology Solar Telescope* (ATST), with first light expected in 2019, will provide imaging and spectroscopic observations of the solar atmosphere from the photosphere to the corona in visible and near-infrared regimes and offer critical plasma and magnetic field diagnostics simultaneously.

References

Afanasyev, A.N., Uralov, A.M.: 2011, *Solar Phys.* **273**, 479. doi:10.1007/s11207-011-9730-9.

Afanasyev, A.N., Uralov, A.M., Grechnev, V.V.: 2013, *Astron. Rep.* **57**, 594. doi:10.1134/S1063772913080015.

Asai, A., Ishii, T.T., Isobe, H., Kitai, R., Ichimoto, K., UeNo, S., Nagata, S., Morita, S., Nishida, K., Shiota, D., Oi, A., Akioka, M., Shibata, K.: 2012, *Astrophys. J. Lett.* **745**, L18. doi:10.1088/2041-8205/745/2/L18.

Aschwanden, M.J.: 2004, *Physics of the Solar Corona. An Introduction*, Praxis, Chichester.

Aschwanden, M.J.: 2009, *Ann. Geophys.* **27**, 3275.

Aschwanden, M.J., Schrijver, C.J.: 2011, *Astrophys. J.* **736**, 102. doi:10.1088/0004-637X/736/2/102.

Aschwanden, M.J., Fletcher, L., Schrijver, C.J., Alexander, D.: 1999, *Astrophys. J.* **520**, 880. doi:10.1086/307502.

Aschwanden, M.J., Boerner, P., Schrijver, C.J., Malanushenko, A.: 2013, *Solar Phys.* **283**, 5. doi:10.1007/s11207-011-9876-5.

Attrill, G.D.R., Harra, L.K., van Driel-Gesztelyi, L., Démoulin, P.: 2007, *Astrophys. J. Lett.* **656**, L101. doi:10.1086/512854.

Bain, H.M., Krucker, S., Glesener, L., Lin, R.P.: 2012, *Astrophys. J.* **750**, 44. doi:10.1088/0004-637X/750/1/44.

Balasubramaniam, K.S., Pevtsov, A.A., Neidig, D.F.: 2007, *Astrophys. J.* **658**, 1372. doi:10.1086/512001.

Balasubramaniam, K.S., Pevtsov, A.A., Neidig, D.F., Cliver, E.W., Thompson, B.J., Young, C.A., Martin, S.F., Kiplinger, A.: 2005, *Astrophys. J.* **630**, 1160. doi:10.1086/432030.

Ballai, I.: 2007, *Solar Phys.* **246**, 177. doi:10.1007/s11207-007-0415-3.

Ballai, I., Douglas, M.: 2008, In: Erdélyi, R., Mendoza-Briceño, C.A. (eds.) *Waves and Oscillations in the Solar Atmosphere: Heating and Magneto-Seismology, IAU Symp.*, Cambridge University Press, Cambridge, **247**, 243. doi:10.1017/S1743921308014932.

Ballai, I., Erdélyi, R., Pintér, B.: 2005, *Astrophys. J. Lett.* **633**, L145. doi:10.1086/498447.

Ballai, I., Forgács-Dajka, E., Douglas, M.: 2011, *Astron. Astrophys.* **527**, A12. doi:10.1051/0004-6361/201016075.

Banerjee, D., Erdélyi, R., Oliver, R., O'Shea, E.: 2007, *Solar Phys.* **246**, 3. doi:10.1007/s11207-007-9029-z.

Becker, U.: 1958, *Zeit. Astrophys.* **44**, 243.

Berger, T.E., Slater, G., Hurlburt, N., Shine, R., Tarbell, T., Title, A., Lites, B.W., Okamoto, T.J., Ichimoto, K., Katsukawa, Y., Magara, T., Suematsu, Y., Shimizu, T.: 2010, *Astrophys. J.* **716**, 1288. doi:10.1088/0004-637X/716/2/1288.

Biesecker, D.A., Myers, D.C., Thompson, B.J., Hammer, D.M., Vourlidas, A.: 2002, *Astrophys. J.* **569**, 1009. doi:10.1086/339402.

Boerner, P.F., Edwards, C.G., Lemen, J.R., Rausch, A., Schrijver, C., Shine, R., Shing, L., Stern, R., Tarbell, T., Title, A., Wolfson, C.J., Soufli, R., Spiller, E., Gullikson, E., McKenzie, D., Windt, D., Golub, L., Podgorski, W., Testa, P., Weber, M.: 2012, *Solar Phys.* **275**, 41. doi:10.1007/s11207-011-9804-8.

Byrne, J.P., Long, D.M., Gallagher, P.T., Bloomfield, D.S., Maloney, S.A., McAteer, R.T.J., Morgan, H., Habbal, S.R.: 2013, *Astron. Astrophys.* **557**, A96. doi:10.1051/0004-6361/201321223.

Carley, E.P., Long, D.M., Byrne, J.P., Zucca, P., Bloomfield, D.S., McCauley, J., Gallagher, P.T.: 2013, *Nature Phys.* **9**, 811. doi:10.1038/nphys2767.

Chen, F., Ding, M.D.: 2010, *Astrophys. J.* **724**, 640. doi:10.1088/0004-637X/724/1/640.

Chen, F., Ding, M.D., Chen, P.F., Harra, L.K.: 2011a, *Astrophys. J.* **740**, 116. doi:10.1088/0004-637X/740/2/116.

Chen, P.F.: 2006, *Astrophys. J. Lett.* **641**, L153. doi:10.1086/503868.

Chen, P.F.: 2011, *Liv. Rev. Solar Phys.* **8**, 1. doi:10.12942/lrsp-2011-1.

Chen, P.F., Wu, Y.: 2011, *Astrophys. J. Lett.* **732**, L20. doi:10.1088/2041-8205/732/2/L20.

Chen, P.F., Ding, M.D., Fang, C.: 2005, *Space Sci. Rev.* **121**, 201. doi:10.1007/s11214-006-3911-0.

Chen, P.F., Fang, C., Shibata, K.: 2005, *Astrophys. J.* **622**, 1202. doi:10.1086/428084.

Chen, P.F., Wu, S.T., Shibata, K., Fang, C.: 2002, *Astrophys. J. Lett.* **572**, L99. doi:10.1086/341486.

Chen, Y., Song, H.Q., Li, B., Xia, L.D., Wu, Z., Fu, H., Li, X.: 2010, *Astrophys. J.* **714**, 644. doi:10.1088/0004-637X/714/1/644.

Chen, Y., Feng, S.W., Li, B., Song, H.Q., Xia, L.D., Kong, X.L., Li, X.: 2011b, *Astrophys. J.* **728**, 147. doi:10.1088/0004-637X/728/2/147.

Cheng, X., Zhang, J., Olmedo, O., Vourlidas, A., Ding, M.D., Liu, Y.: 2012, *Astrophys. J. Lett.* **745**, L5. doi:10.1088/2041-8205/745/1/L5.

Cliver, E.W., Laurenza, M., Storini, M., Thompson, B.J.: 2005, *Astrophys. J.* **631**, 604. doi:10.1086/432250.

Cohen, O., Attrill, G.D.R., Manchester, W.B., Wills-Davey, M.J.: 2009, *Astrophys. J.* **705**, 587. doi:10.1088/0004-637X/705/1/587.

Cooper, F.C., Nakariakov, V.M., Tsiklauri, D.: 2003, *Astron. Astrophys.* **397**, 765. doi:10.1051/0004-6361:20021556.

Cranmer, S.R.: 2012, *Space Sci. Rev.* **172**, 145. doi:10.1007/s11214-010-9674-7.

Culhane, J.L., Harra, L.K., James, A.M., Al-Janabi, K., Bradley, L.J., Chaudry, R.A., Rees, K., Tandy, J.A., Thomas, P., Whillock, M.C.R., Winter, B., Doschek, G.A., Korendyke, C.M., Brown, C.M., Myers, S., Mariska, J., Seely, J., Lang, J., Kent, B.J., Shaughnessy, B.M., Young, P.R., Simnett, G.M., Castelli, C.M., Mahmoud, S., Mapson-Menard, H., Probyn, B.J., Thomas, R.J., Davila, J., Dere, K., Windt, D., Shea, J., Hagood, R., Moye, R., Hara, H., Watanabe, T., Matsuzaki, K., Kosugi, T., Hansteen, V., Wikstol, Ø.: 2007, *Solar Phys.* **243**, 19. doi:10.1007/s01007-007-0293-1.

Dai, Y., Ding, M.D., Chen, P.F., Zhang, J.: 2012, *Astrophys. J.* **759**, 55. doi:10.1088/0004-637X/759/1/55.

De Moortel, I., Ireland, J., Walsh, R.W.: 2000, *Astron. Astrophys.* **355**, L23.

De Pontieu, B., Title, A.M., Lemen, J.R., Kushner, G.D., Akin, D.J., Allard, B., Berger, T., Boerner, P., Cheung, M., Chou, C., Drake, J.F., Duncan, D.W., Freeland, S., Heyman, G.F., Hoffman, C., Hurlburt, N.E., Lindgren, R.W., Mathur, D., Rehse, R., Sabolish, D., Seguin, R., Schrijver, C.J., Tarbell, T.D., Wülser, J.-P., Wolfson, C.J., Yanari, C., Mudge, J., Nguyen-Phuc, N., Timmons, R., van Bezooijen, R., Weingrod, I., Brookner, R., Butcher, G., Dougherty, B., Eder, J., Knagenhjelm, V., Larsen, S., Mansir, D., Phan, L., Boyle, P., Cheimets, P.N., DeLuca, E.E., Golub, L., Gates, R., Hertz, E., McKillop, S., Park, S., Perry, T., Podgorski, W.A., Reeves: 2014, *Solar Phys.*. doi:10.1007/s11207-014-0485-y.

De Rosa, M.L., Schrijver, C.J., Barnes, G., Leka, K.D., Lites, B.W., Aschwanden, M.J., Amari, T., Canou, A., McTiernan, J.M., Régnier, S., Thalmann, J.K., Valori, G., Wheatland, M.S., Wiegelmann, T., Cheung, M.C.M., Conlon, P.A., Fuhrmann, M., Inhester, B., Tadesse, T.: 2009, *Astrophys. J.* **696**, 1780. doi:10.1088/0004-637X/696/2/1780.

DeForest, C.E.: 2004, *Astrophys. J. Lett.* **617**, L89. doi:10.1086/427181.

Delaboudinière, J., Artzner, G.E., Brunaud, J., Gabriel, A.H., Hochedez, J.F., Millier, F., Song, X.Y., Au, B., Dere, K.P., Howard, R.A., Kreplin, R., Michels, D.J., Moses, J.D., Defise, J.M., Jamar, C., Rochus, P., Chauvineau, J.P., Marioge, J.P., Catura, R.C., Lemen, J.R., Shing, L., Stern, R.A., Gurman, J.B., Neupert, W.M., Maucherat, A., Clette, F., Cugnon, P., van Dessel, E.L.: 1995, *Solar Phys.* **162**, 291. doi:10.1007/BF00733432.

Delannée, C.: 2000, *Astrophys. J.* **545**, 512. doi:10.1086/317777.

Delannée, C.: 2009, *Astron. Astrophys.* **495**, 571. doi:10.1051/0004-6361:200809451.

Delannée, C., Aulanier, G.: 1999, *Solar Phys.* **190**, 107. doi:10.1023/A:1005249416605.

Delannée, C., Hochedez, J.-F., Aulanier, G.: 2007, *Astron. Astrophys.* **465**, 603. doi:10.1051/0004-6361:20065845.

Delannée, C., Török, T., Aulanier, G., Hochedez, J.: 2008, *Solar Phys.* **247**, 123. doi:10.1007/s11207-007-9085-4.

Delannée, C., Artzner, G., Schmieder, B., Parenti, S.: 2014, *Solar Phys.*, Online First. doi:10.1007/s11207-014-0488-8.

Dere, K.P., Brueckner, G.E., Howard, R.A., Koomen, M.J., Korendyke, C.M., Kreplin, R.W., Michels, D.J., Moses, J.D., Moulton, N.E., Socker, D.G., St. Cyr, O.C., Delaboudinière, J.P., Artzner, G.E., Brunaud, J., Gabriel, A.H., Hochedez, J.F., Millier, F., Song, X.Y., Chauvineau, J.P., Marioge, J.P., Defise, J.M., Jamar, C., Rochus, P., Catura, R.C., Lemen, J.R., Gurman, J.B., Neupert, W., Clette, F., Cugnon, P., van Dessel, E.L., Lamy, P.L., Llebaria, A., Schwenn, R., Simnett, G.M.: 1997, *Solar Phys.* **175**, 601. doi:10.1023/A:1004907307376.

Dolla, L., Marqué, C., Seaton, D.B., Van Doorsselaere, T., Dominique, M., Berghmans, D., Cabanas, C., De Groof, A., Schmutz, W., Verdini, A., West, M.J., Zender, J., Zhukov, A.N.: 2012, *Astrophys. J. Lett.* **749**, L16. doi:10.1088/2041-8205/749/1/L16.

Downs, C., Roussev, I.I., van der Holst, B., Lugaz, N., Sokolov, I.V., Gombosi, T.I.: 2011, *Astrophys. J.* **728**, 2. doi:10.1088/0004-637X/728/1/2.

Downs, C., Roussev, I.I., van der Holst, B., Lugaz, N., Sokolov, I.V.: 2012, *Astrophys. J.* **750**, 134. doi:10.1088/0004-637X/750/2/134.

Feng, L., Inhester, B., Gan, W.Q.: 2013, *Astrophys. J.* **774**, 141. doi:10.1088/0004-637X/774/2/141.

Feng, S.W., Chen, Y., Li, B., Song, H.Q., Kong, X.L., Xia, L.D., Feng, X.S.: 2011, *Solar Phys.* **272**, 119. doi:10.1007/s11207-011-9814-6.

Fleishman, G.D., Bastian, T.S., Gary, D.E.: 2008, *Astrophys. J.* **684**, 1433. doi:10.1086/589821.

Foullon, C., Verwichte, E., Nakariakov, V.M., Fletcher, L.: 2005, *Astron. Astrophys.* **440**, L59. doi:10.1051/0004-6361:200500169.

Foullon, C., Verwichte, E., Nakariakov, V.M., Nykyri, K., Farrugia, C.J.: 2011, *Astrophys. J. Lett.* **729**, L8. doi:10.1088/2041-8205/729/1/L8.

Foullon, C., Verwichte, E., Nykyri, K., Aschwanden, M.J., Hannah, I.G.: 2013, *Astrophys. J.* **767**, 170. doi:10.1088/0004-637X/767/2/170.

Gallagher, P.T., Long, D.M.: 2011, *Space Sci. Rev.* **158**, 365. doi:10.1007/s11214-010-9710-7.

Gary, D.E., Hurford, G.J.: 1994, *Astrophys. J.* **420**, 903. doi:10.1086/173614.

Gilbert, H.R., Holzer, T.E.: 2004, *Astrophys. J.* **610**, 572. doi:10.1086/421452.

Gilbert, H.R., Holzer, T.E., Thompson, B.J., Burkepile, J.T.: 2004, *Astrophys. J.* **607**, 540. doi:10.1086/383231.

Gopalswamy, N., Thompson, B.J.: 2000, *J. Atmos. Solar-Terr. Phys.* **62**, 1457. doi:10.1016/S1364-6826(00)00079-1.

Gopalswamy, N., Yashiro, S., Krucker, S., Stenborg, G., Howard, R.A.: 2004, *J. Geophys. Res. (Space Phys.)* **109**, 12105. doi:10.1029/2004JA010602.

Gopalswamy, N., Yashiro, S., Xie, H., Akiyama, S., Aguilar-Rodriguez, E., Kaiser, M.L., Howard, R.A., Bougeret, J.-L.: 2008, *Astrophys. J.* **674**, 560. doi:10.1086/524765.

Gopalswamy, N., Yashiro, S., Temmer, M., Davila, J., Thompson, W.T., Jones, S., McAteer, R.T.J., Wuelser, J., Freeland, S., Howard, R.A.: 2009, *Astrophys. J. Lett.* **691**, L123. doi:10.1088/0004-637X/691/2/L123.

Gopalswamy, N., Nitta, N., Akiyama, S., Mäkelä, P., Yashiro, S.: 2012, *Astrophys. J.* **744**, 72. doi:10.1088/0004-637X/744/1/72.

Gopalswamy, N., Xie, H., Mäkelä, P., Yashiro, S., Akiyama, S., Uddin, W., Srivastava, A.K., Joshi, N.C., Chandra, R., Manoharan, P.K., Mahalakshmi, K., Dwivedi, V.C., Jain, R., Awasthi, A.K., Nitta, N.V., Aschwanden, M.J., Choudhary, D.P.: 2013, *Adv. Space Res.* **51**, 1981. doi:10.1016/j.asr.2013.01.006.

Gosain, S., Foullon, C.: 2012, *Astrophys. J.* **761**, 103. doi:10.1088/0004-637X/761/2/103.

Grechnev, V.V., Uralov, A.M., Chertok, I.M., Kuzmenko, I.V., Afanasyev, A.N., Meshalkina, N.S., Kalashnikov, S.S., Kubo, Y.: 2011a, *Solar Phys.* **273**, 433. doi:10.1007/s11207-011-9780-z.

Grechnev, V.V., Afanasyev, A.N., Uralov, A.M., Chertok, I.M., Eselevich, M.V., Eselevich, V.G., Rudenko, G.V., Kubo, Y.: 2011b, *Solar Phys.* **273**, 461. doi:10.1007/s11207-011-9781-y.

Guennou, C., Auchère, F., Soubrié, E., Bocchialini, K., Parenti, S., Barbey, N.: 2012a, *Astrophys. J. Suppl.* **203**, 25. doi:10.1088/0067-0049/203/2/25.

Guennou, C., Auchère, F., Soubrié, E., Bocchialini, K., Parenti, S., Barbey, N.: 2012b, *Astrophys. J. Suppl.* **203**, 26. doi:10.1088/0067-0049/203/2/26.

Habbal, S.R., Druckmüller, M., Morgan, H., Ding, A., Johnson, J., Druckmüllerová, H., Daw, A., Arndt, M.B., Dietzel, M., Saken, J.: 2011, *Astrophys. J.* **734**, 120. doi:10.1088/0004-637X/734/2/120.

Handy, B.N., Acton, L.W., Kankelborg, C.C., Wolfson, C.J., Akin, D.J., Bruner, M.E., Caravalho, R., Catura, R.C., Chevalier, R., Duncan, D.W., Edwards, C.G., Feinstein, C.N., Freeland, S.L., Friedlaender, F.M., Hoffmann, C.H., Hurlburt, N.E., Jurcevich, B.K., Katz, N.L., Kelly, G.A., Lemen, J.R., Levay, M., Lindgren, R.W., Mathur, D.P., Meyer, S.B., Morrison, S.J., Morrison, M.D., Nightingale, R.W., Pope, T.P., Rehse, R.A., Schrijver, C.J., Shine, R.A., Shing, L., Strong, K.T., Tarbell, T.D., Title, A.M., Torgerson, D.D., Golub, L., Bookbinder, J.A., Caldwell, D., Cheimets, P.N., Davis, W.N., Deluca, E.E., McMullen, R.A., Warren, H.P., Amato, D.a.: 1999, *Solar Phys.* **187**, 229. doi:10.1023/A:1005166902804.

Hannah, I.G., Christe, S., Krucker, S., Hurford, G.J., Hudson, H.S., Lin, R.P.: 2008, *Astrophys. J.* **677**, 704. doi:10.1086/529012.

Harra, L.K., Sterling, A.C.: 2003, *Astrophys. J.* **587**, 429. doi:10.1086/368079.

Harra, L.K., Sterling, A.C., Gömöry, P., Veronig, A.: 2011, *Astrophys. J. Lett.* **737**, L4. doi:10.1088/2041-8205/737/1/L4.

Harrison, R.A., Sawyer, E.C., Carter, M.K., Cruise, A.M., Cutler, R.M., Fludra, A., Hayes, R.W., Kent, B.J., Lang, J., Parker, D.J., Payne, J., Pike, C.D., Peskett, S.C., Richards, A.G., Gulhane, J.L., Norman, K., Breeveld, A.A., Breeveld, E.R., Al Janabi, K.F., McCalden, A.J., Parkinson, J.H., Self, D.G., Thomas, P.D., Poland, A.I., Thomas, R.J., Thompson, W.T., Kjeldseth-Moe, O., Brekke, P., Karud, J., Maltby, P., Aschenbach, B., Bräuninger, H., Kühne, M., Hollandt, J., Siegmund, O.H.W., Huber, M.C.E., Gabriel, A.H., Mason, H.E., Bromage, B.J.I.: 1995, *Solar Phys.* **162**, 233. doi:10.1007/BF00733431.

Hershaw, J., Foullon, C., Nakariakov, V.M., Verwichte, E.: 2011, *Astron. Astrophys.* **531**, A53. doi:10.1051/0004-6361/201116750.

Heyvaerts, J., Priest, E.R.: 1983, *Astron. Astrophys.* **117**, 220.

Hoilijoki, S., Pomoell, J., Vainio, R., Palmroth, M., Koskinen, H.E.J.: 2013, *Solar Phys.* **286**, 493. doi:10.1007/s11207-013-0276-x.

Howard, R.A., Moses, J.D., Vourlidas, A., Newmark, J.S., Socker, D.G., Plunkett, S.P., Korendyke, C.M., Cook, J.W., Hurley, A., Davila, J.M., Thompson, W.T., St. Cyr, O.C., Mentzell, E., Mehalick, K., Lemen, J.R., Wuelser, J.P., Duncan, D.W., Tarbell, T.D., Wolfson, C.J., Moore, A., Harrison, R.A., Waltham, N.R., Lang, J., Davis, C.J., Eyles, C.J., Mapson-Menard, H., Simnett, G.M., Halain, J.P., Defise, J.M., Mazy, E., Rochus, P., Mercier, R., Ravet, M.F., Delmotte, F., Auchere, F., Delaboudiniere, J.P., Bothmer, V., Deutsch, W., Wang, D., Rich, N., Cooper, S., Stephens, V., Maahs, G., Baugh, R., McMullin, D., Carter, T.: 2008, *Space Sci. Rev.* **136**, 67. doi:10.1007/s11214-008-9341-4.

Hudson, H.S., Khan, J.I., Lemen, J.R., Nitta, N.V., Uchida, Y.: 2003, *Solar Phys.* **212**, 121. doi:10.1023/A:1022904125479.

Hundhausen, A.J., Sawyer, C.B., House, L., Illing, R.M.E., Wagner, W.J.: 1984, *J. Geophys. Res.* **89**, 2639. doi:10.1029/JA089iA05p02639.

Inglis, A.R., Dennis, B.R.: 2012, *Astrophys. J.* **748**, 139. doi:10.1088/0004-637X/748/2/139.

Innes, D.E., Teriaca, L.: 2013, *Solar Phys.* **282**, 453. doi:10.1007/s11207-012-0199-y.

Innes, D.E., Genetelli, A., Attie, R., Potts, H.E.: 2009, *Astron. Astrophys.* **495**, 319. doi:10.1051/0004-6361:200811011.

Ionson, J.A.: 1978, *Astrophys. J.* **226**, 650. doi:10.1086/156648.

Ireland, J., Marsh, M.S., Kucera, T.A., Young, C.A.: 2010, *Solar Phys.* **264**, 403. doi:10.1007/s11207-010-9592-6.

Ireland, J., Christe, S., Hughitt, V.K., Shih, A.Y., Young, C.A., Earnshaw, M.D., Mayer, F.: 2012, In: *AAS Meeting Abstracts* **220**, 201.17.

Jess, D.B., Mathioudakis, M., Erdélyi, R., Crockett, P.J., Keenan, F.P., Christian, D.J.: 2009, *Science* **323**. doi:10.1126/science.1168680.

Jess, D.B., De Moortel, I., Mathioudakis, M., Christian, D.J., Reardon, K.P., Keys, P.H., Keenan, F.P.: 2012, *Astrophys. J.* **757**, 160. doi:10.1088/0004-637X/757/2/160.

Kaiser, M.L., Kucera, T.A., Davila, J.M., St. Cyr, O.C., Guhathakurta, M., Christian, E.: 2008, *Space Sci. Rev.* **136**, 5. doi:10.1007/s11214-007-9277-0.

Karlický, M., Mészárosová, H., Jelínek, P.: 2013, *Astron. Astrophys.* **550**, A1. doi:10.1051/0004-6361/201220296.

Khan, J.I., Hudson, H.S.: 2000, *Geophys. Res. Lett.* **27**, 1083. doi:10.1029/1999GL010730.

Kienreich, I.W., Temmer, M., Veronig, A.M.: 2009, *Astrophys. J. Lett.* **703**, L118. doi:10.1088/0004-637X/703/2/L118.

Kienreich, I.W., Veronig, A.M., Muhr, N., Temmer, M., Vršnak, B., Nitta, N.: 2011, *Astrophys. J. Lett.* **727**, L43. doi:10.1088/2041-8205/727/2/L43.

Kienreich, I.W., Muhr, N., Veronig, A.M., Berghmans, D., De Groof, A., Temmer, M., Vršnak, B., Seaton, D.B.: 2013, *Solar Phys.* **286**, 201. doi:10.1007/s11207-012-0023-8.

Klassen, A., Aurass, H., Mann, G., Thompson, B.J.: 2000, *Astron. Astrophys. Suppl.* **141**, 357. doi:10.1051/aas:2000125.

Kliem, B., Karlický, M., Benz, A.O.: 2000, *Astron. Astrophys.* **360**, 715.

Kocharov, L.G., Lee, J.W., Zirin, H., Kovaltsov, G.A., Usoskin, I.G., Pyle, K.R., Shea, M.A., Smart, D.F.: 1994, *Solar Phys.* **155**, 149. doi:10.1007/BF00670736.

Kouloumvakos, A., Patsourakos, S., Hillaris, A., Vourlidas, A., Preka-Papadema, P., Moussas, X., Caroubalos, C., Tsitsipis, P., Kontogeorgos, A.: 2014, *Solar Phys.* **289**, 2123. doi:10.1007/s11207-013-0460-z.

Kozarev, K.A., Korreck, K.E., Lobzin, V.V., Weber, M.A., Schwadron, N.A.: 2011, *Astrophys. J. Lett.* **733**, L25. doi:10.1088/2041-8205/733/2/L25.

Kramar, M., Jones, S., Davila, J., Inhester, B., Mierla, M.: 2009, *Solar Phys.* **259**, 109. doi:10.1007/s11207-009-9401-2.

Krucker, S., Larson, D.E., Lin, R.P., Thompson, B.J.: 1999, *Astrophys. J.* **519**, 864. doi:10.1086/307415.

Kumar, P., Manoharan, P.K.: 2013, *Astron. Astrophys.* **553**, A109. doi:10.1051/0004-6361/201220283.

Kumar, P., Cho, K.-S., Chen, P.F., Bong, S.-C., Park, S.-H.: 2013, *Solar Phys.* **282**, 523. doi:10.1007/s11207-012-0158-7.

Kwon, R.-Y., Kramar, M., Wang, T., Ofman, L., Davila, J.M., Chae, J., Zhang, J.: 2013a, *Astrophys. J.* **776**, 55. doi:10.1088/0004-637X/776/1/55.

Kwon, R.-Y., Ofman, L., Olmedo, O., Kramar, M., Davila, J.M., Thompson, B.J., Cho, K.-S.: 2013b, *Astrophys. J.* **766**, 55. doi:10.1088/0004-637X/766/1/55.

Lemen, J.R., Title, A.M., Akin, D.J., Boerner, P.F., Chou, C., Drake, J.F., Duncan, D.W., Edwards, C.G., Friedlaender, F.M., Heyman, G.F., Hurlburt, N.E., Katz, N.L., Kushner, G.D., Levay, M., Lindgren, R.W., Mathur, D.P., McFeaters, E.L., Mitchell, S., Rehse, R.A., Schrijver, C.J., Springer, L.A., Stern, R.A., Tarbell, T.D., Wuelser, J.-P., Wolfson, C.J., Yanari, C., Bookbinder, J.A., Cheimets, P.N., Caldwell, D., Deluca, E.E., Gates, R., Golub, L., Park, S., Podgorski, W.A., Bush, R.I., Scherrer, P.H., Gummin, M.A., Smith, P., Auker, G., Jerram, P., Pool, P., Soufli, R., Windt, D.L., Beardsley, S., Clapp, M., Lang, J., Waltham, N.: 2012, *Solar Phys.* **275**, 17. doi:10.1007/s11207-011-9776-8.

Li, T., Zhang, J., Yang, S.-H., Liu, W.: 2012a, *Res. Astron. Astrophys.* **12**, 104. doi:10.1088/1674-4527/12/1/009.

Li, T., Zhang, J., Yang, S.-H., Liu, W.: 2012b, *Astrophys. J.* **746**, 13. doi:10.1088/0004-637X/746/1/13.

Lin, H., Penn, M.J., Tomczyk, S.: 2000, *Astrophys. J. Lett.* **541**, L83. doi:10.1086/312900.

Liu, R., Liu, C., Xu, Y., Liu, W., Kliem, B., Wang, H.: 2013, *Astrophys. J.* **773**, 166. doi:10.1088/0004-637X/773/2/166.

Liu, W., Berger, T.E., Low, B.C.: 2012, *Astrophys. J. Lett.* **745**, L21. doi:10.1088/2041-8205/745/2/L21.

Liu, W., Chen, Q., Petrosian, V.: 2013, *Astrophys. J.* **767**, 168. doi:10.1088/0004-637X/767/2/168.

Liu, W., Nitta, N.V., Schrijver, C.J., Title, A.M., Tarbell, T.D.: 2010, *Astrophys. J. Lett.* **723**, L53. doi:10.1088/2041-8205/723/1/L53.

Liu, W., Title, A.M., Zhao, J., Ofman, L., Schrijver, C.J., Aschwanden, M.J., De Pontieu, B., Tarbell, T.D.: 2011, *Astrophys. J. Lett.* **736**, L13. doi:10.1088/2041-8205/736/1/L13.

Liu, W., Ofman, L., Nitta, N.V., Aschwanden, M.J., Schrijver, C.J., Title, A.M., Tarbell, T.D.: 2012, *Astrophys. J.* **753**, 52. doi:10.1088/0004-637X/753/1/52.

Liu, W., Ofman, L., Schrijver, C.J., Title, A.M.: 2014a, *to be submitted to Astrophys. J.*

Liu, W., Downs, C., Ofman, L., Title, A.M.: 2014b, *to be submitted to Astrophys. J.*

Liu, W., Ofman, L., Downs, C., Nitta, N.V., Schrijver, C.J.: 2014c, *to be submitted to Astrophys. J.*

Long, D.M., DeLuca, E.E., Gallagher, P.T.: 2011, *Astrophys. J. Lett.* **741**, L21. doi:10.1088/2041-8205/741/1/L21.

Long, D.M., Gallagher, P.T., McAteer, R.T.J., Bloomfield, D.S.: 2008, *Astrophys. J. Lett.* **680**, L81. doi:10.1086/589742.

Long, D.M., Gallagher, P.T., McAteer, R.T.J., Bloomfield, D.S.: 2011, *Astron. Astrophys.* **531**, A42. doi:10.1051/0004-6361/201015879.

Long, D.M., Williams, D.R., Régnier, S., Harra, L.K.: 2013, *Solar Phys.* **288**, 567. doi:10.1007/s11207-013-0331-7.

Long, D.M., Bloomfield, D.S., Gallagher, P.T., Pérez-Suárez, D.: 2014, *Solar Phys.* (accepted), arXiv1403.6722.

Lulić, S., Vršnak, B., Žic, T., Kienreich, I.W., Muhr, N., Temmer, M., Veronig, A.M.: 2013, *Solar Phys.* **286**, 509. doi:10.1007/s11207-013-0287-7.

Ma, S., Wills-Davey, M.J., Lin, J., Chen, P.F., Attrill, G.D.R., Chen, H., Zhao, S., Li, Q., Golub, L.: 2009, *Astrophys. J.* **707**, 503. doi:10.1088/0004-637X/707/1/503.

Ma, S., Raymond, J.C., Golub, L., Lin, J., Chen, H., Grigis, P., Testa, P., Long, D.: 2011, *Astrophys. J.* **738**, 160. doi:10.1088/0004-637X/738/2/160.

Mann, G.: 1995, *Journal of Plasma Physics* **53**, 109. doi:10.1017/S0022377800018043.

Martens, P.C.H., Attrill, G.D.R., Davey, A.R., Engell, A., Farid, S., Grigis, P.C., Kasper, J., Korreck, K., Saar, S.H., Savcheva, A., Su, Y., Testa, P., Wills-Davey, M., Bernasconi, P.N., Raouafi, N.-E., Delouille, V.A., Hochedez, J.F., Cirtain, J.W., Deforest, C.E., Angryk, R.A., de Moortel, I., Wiegelmann, T., Georgoulis, M.K., McAteer, R.T.J., Timmons, R.P.: 2012, *Solar Phys.* **275**, 79. doi:10.1007/s11207-010-9697-y.

McIntosh, S.W., de Pontieu, B., Tomczyk, S.: 2008, *Solar Phys.* **252**, 321. doi:10.1007/s11207-008-9257-x.

McIntosh, S.W., de Pontieu, B., Carlsson, M., Hansteen, V., Boerner, P., Goossens, M.: 2011, *Nature* **475**, 477. doi:10.1038/nature10235.

McLaughlin, J.A., Hood, A.W.: 2004, *Astron. Astrophys.* **420**, 1129. doi:10.1051/0004-6361:20035900.

McLaughlin, J.A., Verth, G., Fedun, V., Erdélyi, R.: 2012, *Astrophys. J.* **749**, 30. doi:10.1088/0004-637X/749/1/30.

Mei, Z., Ziegler, U., Lin, J.: 2012, *Science in China G: Phys. Astron.* **55**, 1316. doi:10.1007/s11433-012-4752-3.

Mészárosová, H., Dudík, J., Karlický, M., Madsen, F.R.H., Sawant, H.S.: 2013, *Solar Phys.*
    283, 473. doi:10.1007/s11207-013-0243-6.

Miteva, R., Klein, K.-L., Kienreich, I., Temmer, M., Veronig, A., Malandraki, O.E.: 2014, *Solar
    Phys.*, Online First. doi:10.1007/s11207-014-0499-5.

Moreton, G.E., Ramsey, H.E.: 1960, *Pub. Astron. Soc. Pac.* **72**, 357. doi:10.1086/127549.

Moses, D., Clette, F., Delaboudinière, J., Artzner, G.E., Bougnet, M., Brunaud, J., Cara-
    betian, C., Gabriel, A.H., Hochedez, J.F., Millier, F., Song, X.Y., Au, B., Dere, K.P.,
    Howard, R.A., Kreplin, R., Michels, D.J., Defise, J.M., Jamar, C., Rochus, P., Chau-
    vineau, J.P., Marioge, J.P., Catura, R.C., Lemen, J.R., Shing, L., Stern, R.A., Gurman,
    J.B., Neupert, W.M., Newmark, J., Thompson, B., Maucherat, A., Portier-Fozzani, F.,
    Berghmans, D., Cugnon, P., van Dessel, E.L., Gabryl, J.R.: 1997, *Solar Phys.* **175**, 571.
    doi:10.1023/A:1004902913117.

Möstl, U.V., Temmer, M., Veronig, A.M.: 2013, *Astrophys. J. Lett.* **766**, L12.
    doi:10.1088/2041-8205/766/1/L12.

Muhr, N., Veronig, A.M., Kienreich, I.W., Temmer, M., Vršnak, B.: 2011, *Astrophys. J.* **739**,
    89. doi:10.1088/0004-637X/739/2/89.

Nakariakov,   V.M.,   Melnikov,   V.F.:   2009,   *Space   Sci.   Rev.*   **149**,   119.
    doi:10.1007/s11214-009-9536-3.

Nakariakov,   V.M.,   Ofman,   L.:   2001,   *Astron.   Astrophys.*   **372**,   L53.
    doi:10.1051/0004-6361:20010607.

Nakariakov, V.M., Verwichte, E.: 2005, *Liv. Rev. Solar Phys.* **2**, 3. doi:10.12942/lrsp-2005-3.

Nakariakov, V.M., Melnikov, V.F., Reznikova, V.E.: 2003, *Astron. Astrophys.* **412**, L7.
    doi:10.1051/0004-6361:20031660.

Nakariakov, V.M., Ofman, L., Deluca, E.E., Roberts, B., Davila, J.M.: 1999, *Science* **285**, 862.
    doi:10.1126/science.285.5429.862.

Narukage, N., Hudson, H.S., Morimoto, T., Akiyama, S., Kitai, R., Kurokawa, H., Shibata,
    K.: 2002, *Astrophys. J. Lett.* **572**, L109. doi:10.1086/341599.

Narukage, N., Ishii, T.T., Nagata, S., UeNo, S., Kitai, R., Kurokawa, H., Akioka, M., Shibata,
    K.: 2008, *Astrophys. J. Lett.* **684**, L45. doi:10.1086/592108.

Nitta, N.V.: 2012, In: Heerikhuisen, J., Li, G., Pogorelov, N., Zank, G. (eds.) *Physics of the
    Heliosphere: A 10 Year Retrospective: Proceedings of the 10th Annual International As-
    trophysics Conference, Ameri. Inst. Phys. Conf. Sers.* **1436**, 259. doi:10.1063/1.4723617.

Nitta, N.V., Liu, Y., DeRosa, M.L., Nightingale, R.W.: 2012, *Space Sci. Rev.* **171**, 61.
    doi:10.1007/s11214-012-9877-1.

Nitta, N.V., Schrijver, C.J., Title, A.M., Liu, W.: 2013, *Astrophys. J.* **776**, 58.
    doi:10.1088/0004-637X/776/1/58.

Nitta, N.V., Liu, W., Gopalswamy, N., Yashiro, S.: 2014a, *to be submitted to Solar Phys.*

Nitta, N.V., Aschwanden, M.J., Freeland, S.L., Lemen, J.R., Wülser, J.-P., Zarro, D.M.: 2014b,
    Solar Phys. **289**, 1257. doi:10.1007/s11207-013-0388-3.

Nykyri, K., Foullon, C.: 2013, *Geophys. Res. Lett.* **40**, 4154. doi:10.1002/grl.50807.

O'Dwyer, B., Del Zanna, G., Mason, H.E., Weber, M.A., Tripathi, D.: 2010, *Astron. Astrophys.*
    521, A21. doi:10.1051/0004-6361/201014872.

Ofman, L.: 2007, *Astrophys. J.* **655**, 1134. doi:10.1086/510012.

Ofman, L.: 2009, *Space Sci. Rev.* **149**, 153. doi:10.1007/s11214-009-9501-1.

Ofman, L.: 2010, *Liv. Rev. Solar Phys.* **7**, 4. doi:10.12942/lrsp-2010-4.

Ofman, L., Davila, J.M.: 1995, *J. Geophys. Res.* **100**, 23413. doi:10.1029/95JA02222.

Ofman, L., Sui, L.: 2006, *Astrophys. J. Lett.* **644**, L149. doi:10.1086/505622.

Ofman, L., Thompson, B.J.: 2002, *Astrophys. J.* **574**, 440. doi:10.1086/340924.

Ofman, L., Thompson, B.J.: 2010, *AGU Fall Meeting Abstracts*, A2.

Ofman,   L.,   Thompson,   B.J.:   2011,   *Astrophys.   J.   Lett.*   **734**,   L11.
    doi:10.1088/2041-8205/734/1/L11.

Ofman, L., Romoli, M., Poletto, G., Noci, G., Kohl, J.L.: 1997, *Astrophys. J. Lett.* **491**, L111.
    doi:10.1086/311067.

Ofman, L., Liu, W., Title, A., Aschwanden, M.: 2011, *Astrophys. J. Lett.* **740**, L33.
    doi:10.1088/2041-8205/740/2/L33.

Okamoto, T.J., Nakai, H., Keiyama, A., Narukage, N., UeNo, S., Kitai, R., Kurokawa, H.,
    Shibata, K.: 2004, *Astrophys. J.* **608**, 1124. doi:10.1086/420838.

Olmedo, O., Vourlidas, A., Zhang, J., Cheng, X.: 2012, *Astrophys. J.* **756**, 143.
    doi:10.1088/0004-637X/756/2/143.

Park, J., Innes, D.E., Bucik, R., Moon, Y.-J.: 2013, *Astrophys. J.* **779**, 184.
    doi:10.1088/0004-637X/779/2/184.

Pascoe, D.J., Nakariakov, V.M., Kupriyanova, E.G.: 2013, *Astron. Astrophys.* **560**, A97. doi:10.1051/0004-6361/201322678.

Patsourakos, S., Vourlidas, A.: 2009, *Astrophys. J. Lett.* **700**, L182. doi:10.1088/0004-637X/700/2/L182.

Patsourakos, S., Vourlidas, A.: 2012, *Solar Phys.* **281**, 187. doi:10.1007/s11207-012-9988-6.

Patsourakos, S., Vourlidas, A., Kliem, B.: 2010, *Astron. Astrophys.* **522**, A100. doi:10.1051/0004-6361/200913599.

Patsourakos, S., Vourlidas, A., Stenborg, G.: 2010, *Astrophys. J. Lett.* **724**, L188. doi:10.1088/2041-8205/724/2/L188.

Patsourakos, S., Vourlidas, A., Wang, Y.M., Stenborg, G., Thernisien, A.: 2009, *Solar Phys.* **259**, 49. doi:10.1007/s11207-009-9386-x.

Pearce, G., Harrison, R.A.: 1990, *Astron. Astrophys.* **228**, 513.

Pesnell, W.D., Thompson, B.J., Chamberlin, P.C.: 2012, *Solar Phys.* **275**, 3. doi:10.1007/s11207-011-9841-3.

Podladchikova, O., Berghmans, D.: 2005, *Solar Phys.* **228**, 265. doi:10.1007/s11207-005-5373-z.

Podladchikova, O., Vourlidas, A., Van der Linden, R.A.M., Wülser, J.-P., Patsourakos, S.: 2010, *Astrophys. J.* **709**, 369. doi:10.1088/0004-637X/709/1/369.

Podladchikova, O., Vuets, A., Leontiev, P., van der Linden, R.A.M.: 2012, *Solar Phys.* **276**, 479. doi:10.1007/s11207-011-9894-3.

Pomoell, J., Vainio, R., Kissmann, R.: 2008, *Solar Phys.* **253**, 249. doi:10.1007/s11207-008-9186-8.

Reames, D.V.: 2013, *Space Sci. Rev.* **175**, 53. doi:10.1007/s11214-013-9958-9.

Roberts, B.: 2008, In: Erdélyi, R., Mendoza-Briceño, C.A. (eds.) *Waves and Oscillations in the Solar Atmosphere: Heating and Magneto-Seismology, IAU Symp.*, Cambridge University Press, Cambridge, **247**, 3. doi:10.1017/S1743921308014609.

Roberts, B., Edwin, P.M., Benz, A.O.: 1984, *Astrophys. J.* **279**, 857. doi:10.1086/161956.

Rouillard, A.P., Odstrcil, D., Sheeley, N.R., Tylka, A., Vourlidas, A., Mason, G., Wu, C.-C., Savani, N.P., Wood, B.E., Ng, C.K., Stenborg, G., Szabo, A., St. Cyr, O.C.: 2011, *Astrophys. J.* **735**, 7. doi:10.1088/0004-637X/735/1/7.

Rouillard, A.P., Sheeley, N.R., Tylka, A., Vourlidas, A., Ng, C.K., Rakowski, C., Cohen, C.M.S., Mewaldt, R.A., Mason, G.M., Reames, D., Savani, N.P., St. Cyr, O.C., Szabo, A.: 2012, *Astrophys. J.* **752**, 44. doi:10.1088/0004-637X/752/1/44.

Roussev, I.I., Gombosi, T.I., Sokolov, I.V., Velli, M., Manchester, W. IV, DeZeeuw, D.L., Liewer, P., Tóth, G., Luhmann, J.: 2003, *Astrophys. J. Lett.* **595**, L57. doi:10.1086/378878.

Ryutova, M., Berger, T., Frank, Z., Tarbell, T., Title, A.: 2010, *Solar Phys.* **267**, 75. doi:10.1007/s11207-010-9638-9.

Sakai, J.-I., Washimi, H.: 1982, *Astrophys. J.* **258**, 823. doi:10.1086/160129.

Santandrea, S., Gantois, K., Strauch, K., Teston, F., Tilmans, E., Baijot, C., Gerrits, D., De Groof, A., Schwehm, G., Zender, J.: 2013, *Solar Phys.* **286**, 5. doi:10.1007/s11207-013-0289-5.

Schmelz, J.T., Jenkins, B.S., Worley, B.T., Anderson, D.J., Pathak, S., Kimble, J.A.: 2011, *Astrophys. J.* **731**, 49. doi:10.1088/0004-637X/731/1/49.

Schmidt, J.M., Ofman, L.: 2010, *Astrophys. J.* **713**, 1008. doi:10.1088/0004-637X/713/2/1008.

Schrijver, C.J.: 2010, *Astrophys. J.* **710**, 1480. doi:10.1088/0004-637X/710/2/1480.

Schrijver, C.J., Title, A.M.: 2011, *J. Geophys. Res. (Space Phys.)* **116**, 4108. doi:10.1029/2010JA016224.

Schrijver, C.J., Aulanier, G., Title, A.M., Pariat, E., Delannée, C.: 2011, *Astrophys. J.* **738**, 167. doi:10.1088/0004-637X/738/2/167.

Schrijver, C.J., Title, A.M., Yeates, A.R., DeRosa, M.L.: 2013, *Astrophys. J.* **773**, 93. doi:10.1088/0004-637X/773/2/93.

Schwenn, R.: 1996, *Astrophys. Space Sci.* **243**, 187. doi:10.1007/BF00644053.

Seaton, D.B., Berghmans, D., Nicula, B., Halain, J.-P., De Groof, A., Thibert, T., Bloomfield, D.S., Raftery, C.L., Gallagher, P.T., Auchère, F., Defise, J.-M., D'Huys, E., Lecat, J.-H., Mazy, E., Rochus, P., Rossi, L., Schühle, U., Slemzin, V., Yalim, M.S., Zender, J.: 2013, *Solar Phys.* **286**, 43. doi:10.1007/s11207-012-0114-6.

Selwa, M., Poedts, S., DeVore, C.R.: 2012, *Astrophys. J. Lett.* **747**, L21. doi:10.1088/2041-8205/747/2/L21.

Selwa, M., Poedts, S., DeVore, C.R.: 2013, *Solar Phys.* **284**, 515. doi:10.1007/s11207-013-0302-z.

Shen, Y., Liu, Y.: 2012a, *Astrophys. J.* **754**, 7. doi:10.1088/0004-637X/754/1/7.

Shen, Y., Liu, Y.: 2012b, *Astrophys. J.* **753**, 53. doi:10.1088/0004-637X/753/1/53.

Shen, Y., Liu, Y.: 2012c, *Astrophys. J. Lett.* **752**, L23. doi:10.1088/2041-8205/752/2/L23.

Shen, Y.-D., Liu, Y., Su, J.-T., Li, H., Zhang, X.-F., Tian, Z.-J., Zhao, R.-J., Elmhamdi, A.: 2013a, *Solar Phys.* **288**, 585. doi:10.1007/s11207-013-0395-4.

Shen, Y., Liu, Y., Su, J., Li, H., Zhao, R., Tian, Z., Ichimoto, K., Shibata, K.: 2013b, *Astrophys. J. Lett.* **773**, L33. doi:10.1088/2041-8205/773/2/L33.

Soler, R., Díaz, A.J., Ballester, J.L., Goossens, M.: 2012, *Astrophys. J.* **749**, 163. doi:10.1088/0004-637X/749/2/163.

Srivastava, A.K., Goossens, M.: 2013, *Astrophys. J.* **777**, 17. doi:10.1088/0004-637X/777/1/17.

Su, J.T., Shen, Y.D., Liu, Y., Liu, Y., Mao, X.J.: 2012, *Astrophys. J.* **755**, 113. doi:10.1088/0004-637X/755/2/113.

Sych, R.A., Nakariakov, V.M., Anfinogentov, S.A., Ofman, L.: 2010, *Solar Phys.* **266**, 349. doi:10.1007/s11207-010-9616-2.

Sych, R., Nakariakov, V.M., Karlicky, M., Anfinogentov, S.: 2009, *Astron. Astrophys.* **505**, 791. doi:10.1051/0004-6361/200912132.

Temmer, M., Vršnak, B., Veronig, A.M.: 2013, *Solar Phys.* **287**, 441. doi:10.1007/s11207-012-0088-4.

Temmer, M., Vršnak, B., Žic, T., Veronig, A.M.: 2009, *Astrophys. J.* **702**, 1343. doi:10.1088/0004-637X/702/2/1343.

Temmer, M., Veronig, A.M., Gopalswamy, N., Yashiro, S.: 2011, *Solar Phys.* **273**, 421. doi:10.1007/s11207-011-9746-1.

Terradas, J., Ofman, L.: 2004, *Astrophys. J.* **610**, 523. doi:10.1086/421514.

Thompson, B.J., Myers, D.C.: 2009, *Astrophys. J. Suppl.* **183**, 225. doi:10.1088/0067-0049/183/2/225.

Thompson, B.J., Plunkett, S.P., Gurman, J.B., Newmark, J.S., St. Cyr, O.C., Michels, D.J.: 1998, *Geophys. Res. Lett.* **25**, 2465. doi:10.1029/98GL50429.

Thompson, B.J., Gurman, J.B., Neupert, W.M., Newmark, J.S., Delaboudinière, J., St. Cyr, O.C., Stezelberger, S., Dere, K.P., Howard, R.A., Michels, D.J.: 1999, *Astrophys. J. Lett.* **517**, L151. doi:10.1086/312030.

Thompson, B.J., Reynolds, B., Aurass, H., Gopalswamy, N., Gurman, J.B., Hudson, H.S., Martin, S.F., St. Cyr, O.C.: 2000, *Solar Phys.* **193**, 161.

Threlfall, J., De Moortel, I., McIntosh, S.W., Bethge, C.: 2013, *Astron. Astrophys.* **556**, A124. doi:10.1051/0004-6361/201321782.

Tomczyk, S., McIntosh, S.W.: 2009, *Astrophys. J.* **697**, 1384. doi:10.1088/0004-637X/697/2/1384.

Tomczyk, S., McIntosh, S.W., Keil, S.L., Judge, P.G., Schad, T., Seeley, D.H., Edmondson, J.: 2007, *Science* **317**. doi:10.1126/science.1143304.

Torsti, J., Kocharov, L.G., Teittinen, M., Thompson, B.J.: 1999, *Astrophys. J.* **510**, 460. doi:10.1086/306581.

Tripathi, D., Raouafi, N.-E.: 2007, *Astron. Astrophys.* **473**, 951. doi:10.1051/0004-6361:20077255.

Uchida, Y.: 1968, *Solar Phys.* **4**, 30. doi:10.1007/BF00146996.

Uchida, Y.: 1970, *Pub. Astron. Soc. Japan* **22**, 341.

Uchida, Y.: 1974, *Solar Phys.* **39**, 431. doi:10.1007/BF00162436.

Žic, T., Vršnak, B., Temmer, M., Jacobs, C.: 2008, *Solar Phys.* **253**, 237. doi:10.1007/s11207-008-9173-0.

Veronig, A.M., Temmer, M., Vršnak, B.: 2008, *Astrophys. J. Lett.* **681**, L113. doi:10.1086/590493.

Veronig, A.M., Temmer, M., Vršnak, B., Thalmann, J.K.: 2006, *Astrophys. J.* **647**, 1466. doi:10.1086/505456.

Veronig, A.M., Muhr, N., Kienreich, I.W., Temmer, M., Vršnak, B.: 2010, *Astrophys. J. Lett.* **716**, L57. doi:10.1088/2041-8205/716/1/L57.

Veronig, A.M., Gomory, P., Kienreich, I.W., Muhr, N., Vršnak, B., Temmer, M., Warren, H.P.: 2011, *Astrophys. J. Lett.* **743**, L10.

Verwichte, E., Nakariakov, V.M., Cooper, F.C.: 2005, *Astron. Astrophys.* **430**, L65. doi:10.1051/0004-6361:200400133.

Vršnak, B., Cliver, E.W.: 2008, *Solar Phys.* **253**, 215. doi:10.1007/s11207-008-9241-5.

Vršnak, B., Lulić, S.: 2000, *Solar Phys.* **196**, 157. doi:10.1023/A:1005236804727.

Vršnak, B., Warmuth, A., Brajša, R., Hanslmeier, A.: 2002, *Astron. Astrophys.* **394**, 299. doi:10.1051/0004-6361:20021121.

Vršnak, B., Magdalenić, J., Temmer, M., Veronig, A., Warmuth, A., Mann, G., Aurass, H., Otruba, W.: 2005, *Astrophys. J. Lett.* **625**, L67. doi:10.1086/430763.

Wang, H., Shen, C., Lin, J.: 2009, *Astrophys. J.* **700**, 1716. doi:10.1088/0004-637X/700/2/1716.

Wang, T., Ofman, L., Davila, J.M., Su, Y.: 2012, *Astrophys. J. Lett.* **751**, L27. doi:10.1088/2041-8205/751/2/L27.

Wang, Y.: 2000, *Astrophys. J. Lett.* **543**, L89. doi:10.1086/318178.

Warmuth, A.: 2007, In: Klein, K.-L., MacKinnon, A.L. (eds.) *Lecture Notes in Physics*, Springer, Berlin, **725**, 107.

Warmuth, A.: 2010, *Adv. Space Res.* **45**, 527. doi:10.1016/j.asr.2009.08.022.

Warmuth, A., Mann, G.: 2005, *Astron. Astrophys.* **435**, 1123. doi:10.1051/0004-6361:20042169.

Warmuth, A., Mann, G.: 2011, *Astron. Astrophys.* **532**, A151. doi:10.1051/0004-6361/201116685.

Warmuth, A., Vršnak, B., Aurass, H., Hanslmeier, A.: 2001, *Astrophys. J. Lett.* **560**, L105. doi:10.1086/324055.

Warmuth, A., Vršnak, B., Magdalenić, J., Hanslmeier, A., Otruba, W.: 2004, *Astron. Astrophys.* **418**, 1101. doi:10.1051/0004-6361:20034332.

Weber, M.A., Deluca, E.E., Golub, L., Sette, A.L.: 2004, In: Stepanov, A.V., Benevolenskaya, E.E., Kosovichev, A.G. (eds.) *Multi-Wavelength Investigations of Solar Activity, IAU Symp.*, Cambridge University Press, Cambridge, **223**, 321. doi:10.1017/S1743921304006088.

West, M.J., Zhukov, A.N., Dolla, L., Rodriguez, L.: 2011, *Astrophys. J.* **730**, 122. doi:10.1088/0004-637X/730/2/122.

White, R.S., Verwichte, E.: 2012, *Astron. Astrophys.* **537**, A49. doi:10.1051/0004-6361/201118093.

White, S.M., Kundu, M.R.: 1997, *Solar Phys.* **174**, 31. doi:10.1023/A:1004975528106.

White, S.M., Thompson, B.J.: 2005, *Astrophys. J. Lett.* **620**, L63. doi:10.1086/428428.

White, S.M., Balasubramanian, K.S., Cliver, E.W.: 2011, *AAS/Solar Physics Division Abstracts #42*, 1307.

Williams, D.R., Mathioudakis, M., Gallagher, P.T., Phillips, K.J.H., McAteer, R.T.J., Keenan, F.P., Rudawy, P., Katsiyannis, A.C.: 2002, *Mon. Not. Roy. Astron. Soc.* **336**, 747. doi:10.1046/j.1365-8711.2002.05764.x.

Wills-Davey, M.J.: 2003, Propagating disturbances in the lower solar corona. PhD thesis, Montana State University.

Wills-Davey, M.J.: 2006, *Astrophys. J.* **645**, 757. doi:10.1086/504144.

Wills-Davey, M.J., Attrill, G.D.R.: 2009, *Space Sci. Rev.* **149**, 325. doi:10.1007/s11214-009-9612-8.

Wills-Davey, M.J., Thompson, B.J.: 1999, *Solar Phys.* **190**, 467. doi:10.1023/A:1005201500675.

Wills-Davey, M.J., DeForest, C.E., Stenflo, J.O.: 2007, *Astrophys. J.* **664**, 556. doi:10.1086/519013.

Withbroe, G.L., Noyes, R.W.: 1977, *Annu. Rev. Astron. Astrophys.* **15**, 363. doi:10.1146/annurev.aa.15.090177.002051.

Wu, S.T., Zheng, H., Wang, S., Thompson, B.J., Plunkett, S.P., Zhao, X.P., Dryer, M.: 2001, *J. Geophys. Res.* **106**, 25089. doi:10.1029/2000JA000447.

Wuelser, J.-P., Lemen, J.R., Tarbell, T.D., Wolfson, C.J., Cannon, J.C., Carpenter, B.A., Duncan, D.W., Gradwohl, G.S., Meyer, S.B., Moore, A.S., Navarro, R.L., Pearson, J.D., Rossi, G.R., Springer, L.A., Howard, R.A., Moses, J.D., Newmark, J.S., Delaboudiniere, J.-P., Artzner, G.E., Auchere, F., Bougnet, M., Bouyries, P., Bridou, F., Clotaire, J.-Y., Colas, G., Delmotte, F., Jerome, A., Lamare, M., Mercier, R., Mullot, M., Ravet, M.-F., Song, X., Bothmer, V., Deutsch, W.: 2004, In: Fineschi, S., Gummin, M.A. (eds.) *SPIECS* **5171**, 111. doi:10.1117/12.506877.

Xue, Z.K., Qu, Z.Q., Yan, X.L., Zhao, L., Ma, L.: 2013, *Astron. Astrophys.* **556**, A152. doi:10.1051/0004-6361/201220731.

Yang, L., Zhang, J., Liu, W., Li, T., Shen, Y.: 2013, *Astrophys. J.* **775**, 39. doi:10.1088/0004-637X/775/1/39.

Yuan, D., Nakariakov, V.M.: 2012, *Astron. Astrophys.* **543**, A9. doi:10.1051/0004-6361/201218848.

Yuan, D., Shen, Y., Liu, Y., Nakariakov, V.M., Tan, B., Huang, J.: 2013, *Astron. Astrophys.* **554**, A144. doi:10.1051/0004-6361/201321435.

Zaqarashvili, T.V., Vörös, Z., Zhelyazkov, I.: 2014, *Astron. Astrophys.* **561**, A62. doi:10.1051/0004-6361/201322808.

Zaqarashvili, T.V., Melnik, V.N., Brazhenko, A.I., Panchenko, M., Konovalenko, A.A., Franzuzenko, A.V., Dorovskyy, V.V., Rucker, H.O.: 2013, *Astron. Astrophys.* **555**, A55. doi:10.1051/0004-6361/201321548.

Zhang, J., Liu, Y.: 2011, *Astrophys. J. Lett.* **741**, L7. doi:10.1088/2041-8205/741/1/L7.

Zhang, Y., Kitai, R., Narukage, N., Matsumoto, T., Ueno, S., Shibata, K., Wang, J.: 2011, *Pub. Astron. Soc. Japan* **63**.

Zhao, X., Hoeksema, J.T.: 1994, *Solar Phys.* **151**, 91. doi:10.1007/BF00654084.

Zhao, X.H., Wu, S.T., Wang, A.H., Vourlidas, A., Feng, X.S., Jiang, C.W.: 2011, *Astrophys. J.* **742**, 131. doi:10.1088/0004-637X/742/2/131.

Zheng, R.-S., Jiang, Y.-C., Yang, J.-Y., Hong, J.-C., Bi, Y., Yang, B., Yang, D.: 2013a, *Mon. Not. Roy. Astron. Soc.* **431**, 1359. doi:10.1093/mnras/stt258.

Zheng, R., Jiang, Y., Hong, J., Yang, J., Bi, Y., Yang, L., Yang, D.: 2011, *Astrophys. J. Lett.* **739**, L39. doi:10.1088/2041-8205/739/2/L39.

Zheng, R., Jiang, Y., Yang, J., Bi, Y., Hong, J., Yang, D., Yang, B.: 2012a, *Astrophys. J.* **753**, 112. doi:10.1088/0004-637X/753/2/112.

Zheng, R., Jiang, Y., Yang, J., Bi, Y., Hong, J., Yang, B., Yang, D.: 2012b, *Astron. Astrophys.* **541**, A49. doi:10.1051/0004-6361/201118305.

Zheng, R., Jiang, Y., Yang, J., Bi, Y., Hong, J., Yang, D., Yang, B.: 2012c, *Astrophys. J. Lett.* **753**, L29. doi:10.1088/2041-8205/753/2/L29.

Zheng, R., Jiang, Y., Yang, J., Bi, Y., Hong, J., Yang, B., Yang, D.: 2012d, *Astrophys. J.* **747**, 67. doi:10.1088/0004-637X/747/1/67.

Zheng, R., Jiang, Y., Yang, J., Bi, Y., Hong, J., Yang, B., Yang, D.: 2013b, *Astrophys. J.* **764**, 70. doi:10.1088/0004-637X/764/1/70.

Zhukov, A.N.: 2011, *J. Atmos. Solar-Terr. Phys.* **73**, 1096. doi:10.1016/j.jastp.2010.11.030.

Zhukov, A.N., Auchère, F.: 2004, *Astron. Astrophys.* **427**, 705. doi:10.1051/0004-6361:20040351.

Zhukov, A.N., Veselovsky, I.S.: 2007, *Astrophys. J. Lett.* **664**, L131. doi:10.1086/520928.

Zhukov, A.N., Rodriguez, L., de Patoul, J.: 2009, *Solar Phys.* **259**, 73. doi:10.1007/s11207-009-9375-0.

Zucca, P., Carley, E.P., Bloomfield, D.S., Gallagher, P.T.: 2014, *Astron. Astrophys.* (accepted), arXiv1402.4051.